

MARSHALL, MICHAEL M., Ph.D. Solid-State Nanopores: A New Platform for DNA Biomarker Discovery. (2014)  
Directed by Dr. Adam R. Hall. 76 pp.

Solid-state (SS) nanopores emerged as a molecular detection platform in 2001, offering many advantages over their biological counterparts,  $\alpha$ -hemolysin nanopores ( $\alpha$ -HL). These advantages include better chemical, electrical, mechanical, and thermal stability, as well as size tunability and device integration. In addition, the size of  $\alpha$ -HL restricts its application to translocations of single-stranded polynucleotides (ssDNA and ssRNA). This research project focused on developing a SS-nanopore platform for biomarker detection, based on differentiating ssDNA and double-stranded DNA (dsDNA) at the single-molecule scale. Reported dsDNA translocation measurements result in an average residence time of  $\sim 30$  ns/bp, so the temporal resolution required for detection of small DNA duplexes can exceed available bandwidth limitations. To address this issue, several system parameters were explored in order to slow down translocation speed, thereby increasing temporal resolution and signal-to-noise ratio. These parameters included: applied voltage, pH, pore geometry, DNA binding agents, salt composition and concentration, and temperature. Experimental findings showed that SS-nanopores can be precisely fabricated using a controlled helium ion milling technique, acidic conditions cause DNA depurination that results in slower translocation durations, and single-stranded binding proteins (SSBs) bind preferentially to ssDNA, forming complexes with

distinct translocation characteristics that permit large (> 7 kb) ds- and ssDNA to be effectively distinguished. Together, these data show that SS-nanopores can serve as a tool to electronically detect the presence and relative concentration of target DNA molecules with ultrahigh sensitivity, thus demonstrating their potential utility as a biomarker discovery platform in both biomedical and environmental applications.



SOLID-STATE NANOPORES: A NEW PLATFORM FOR DNA  
BIOMARKER DISCOVERY

by

Michael M. Marshall

A Dissertation Submitted to  
the Faculty of the Graduate School at  
The University of North Carolina at Greensboro  
in Partial Fulfillment  
of the Requirements for the Doctor of Philosophy

Greensboro  
2014

Approved by

---

Committee Chair

APPROVAL PAGE

This dissertation written by Michael M. Marshall has been approved by the following committee of the Faculty of the Graduate School at The University of North Carolina at Greensboro.

Committee Chair \_\_\_\_\_

Committee Members \_\_\_\_\_

\_\_\_\_\_

\_\_\_\_\_

\_\_\_\_\_

\_\_\_\_\_  
Date of Acceptance by Committee

\_\_\_\_\_  
Date of Final Oral Examination

## TABLE OF CONTENTS

	Page
LIST OF FIGURES .....	iv
CHAPTER	
I. INTRODUCTION .....	1
Nanopore Research Background .....	1
Conditions to Increase DNA Translocation Times .....	9
II. MATERIALS AND METHODS.....	16
Membrane Thinning Techniques for Nanopore Fabrication .....	16
Solid-State Nanopore Translocation Measurements .....	17
III. MEMBRANE THINNING TECHNIQUES FOR NANOPORE FABRICATION.....	20
Introduction .....	20
Experimental Methods .....	21
Results.....	24
Discussion .....	28
IV. DETECTING DNA DEPURINATION.....	30
Introduction .....	30
Experimental Methods .....	33
Results and Discussion .....	35
V. USING SINGLE-STRANDED BINDING PROTEINS TO DIFFERENTIATE DOUBLE- AND SINGLE-STRANDED DNA .....	43
Introduction .....	43
Experimental Methods .....	46
Results and Discussion .....	49
VI. CONCLUSIONS .....	63
REFERENCES .....	68

## LIST OF FIGURES

	Page
Figure 1.1. SS-nanopore translocation measurements .....	3
Figure 1.2. Applied voltage versus mean conductance blockade .....	5
Figure 1.3. Example SS-nanopore translocation events .....	6
Figure 1.4. Dye intercalation of dsDNA .....	7
Figure 1.5. SS-nanopore discrimination of monobiotinylated dsDNA.....	9
Figure 1.6. Using salt to slow down DNA translocations .....	11
Figure 1.7. pH versus current blockage for 3 kbp dsDNA .....	13
Figure 1.8. Discriminating small nucleic acids using thin SS-nanopores .....	15
Figure 2.1. Experimental setup.....	17
Figure 2.2. Diagram of SS-nanopore Device.....	18
Figure 3.1. Experimental setup.....	22
Figure 3.2. Images of ion-milled patterns .....	23
Figure 3.3. Topographical measurements of direct- and transmission- milled surfaces.....	26
Figure 3.4. Ion milling depth analysis .....	27
Figure 4.1. SS-nanopore detection of DNA depurination .....	32
Figure 4.2. Conductance blockade depth across the pH range .....	36
Figure 4.3. Event durations across the pH range .....	38
Figure 4.4. Gel analysis of DNA across a pH range.....	40
Figure 4.5. Isolating structural factors from solvent effects .....	42

Figure 5.1. SS-nanopore detection of the DNA-SSB complex .....	46
Figure 5.2. Event duration versus mean conductance blockade for 61-mer DNA and SSB .....	51
Figure 5.3. Gel analysis of 61-mer ssDNA mixed with SSB .....	52
Figure 5.4. Diagram of the (SSB) <sub>65</sub> binding mode .....	55
Figure 5.5. Titration series mixtures of ssDNA+SSB.....	57
Figure 5.6. Comparison of dsDNA and ssDNA+SSB .....	58
Figure 5.7. Circular ssDNA+SSB and linearized ssDNA+SSB.....	62

# CHAPTER I

## INTRODUCTION

### Nanopore Research Background

The concept of nanopore sensing evolved from an orifice-based resistive counter, invented by Wallace Coulter in the 1940's. Although the original counter was simply a tiny hole punched through a cellophane cigarette wrapper (1), it led to the more sophisticated device known as a Coulter counter, still in use today, which is used to count and size red blood cells. However, particle detection limits are restricted to the micrometer range.

The advent of nanopores began with the isolation of *Staphylococcus aureus*  $\alpha$ -hemolysin ( $\alpha$ -HL) toxins, natural proteins that self-assemble into membrane channels through lipid bilayers (2). Although these biological nanopores provided the first demonstrations of single biomolecule measurements, their invariant size limits their application to analytes which can fit through a 2 nm diameter, such as single-stranded nucleic acids.

Nearly a decade later, the first solid-state nanopores (SS-nanopores) were introduced in 2001 after technological advances made it possible to use transmission electron microscopes to fabricate nanoscale apertures in thin, insulating membranes, such as silicon oxide (SiO<sub>2</sub>) or silicon nitride (SiN) (3). SS-nanopores are more versatile than their biological counterparts, offering greater

chemical, electrical, mechanical, and thermal stability. These material characteristics also make it possible to tune their size with precision and integrate them with other device components. Although both biological and synthetic nanopore technologies provide unprecedented detection capabilities down to the single molecule scale, at least a thousand-fold greater than Coulter counters.

The fundamental working principle behind nanopore sensing is very straightforward. When a voltage is applied across a nanoscale aperture in an electrolytic solution, it generates an electric field and produces a steady DC current that remains constant and serves as a baseline current signal (1). A charged particle or biopolymer that is captured by the electric field is drawn into and through the nanopore in a process known as a translocation event (Fig. 1.1a). Each biomolecule displaces an equal volume of solution as it migrates electrokinetically through the SS-nanopore, causing the current to drop by an amount that is proportional to its own volume (4). The electrical feedback associated with these current changes appears as a series of resistive pulses which provide spatial and temporal information about the translocating biomolecules (Fig. 1.1b).

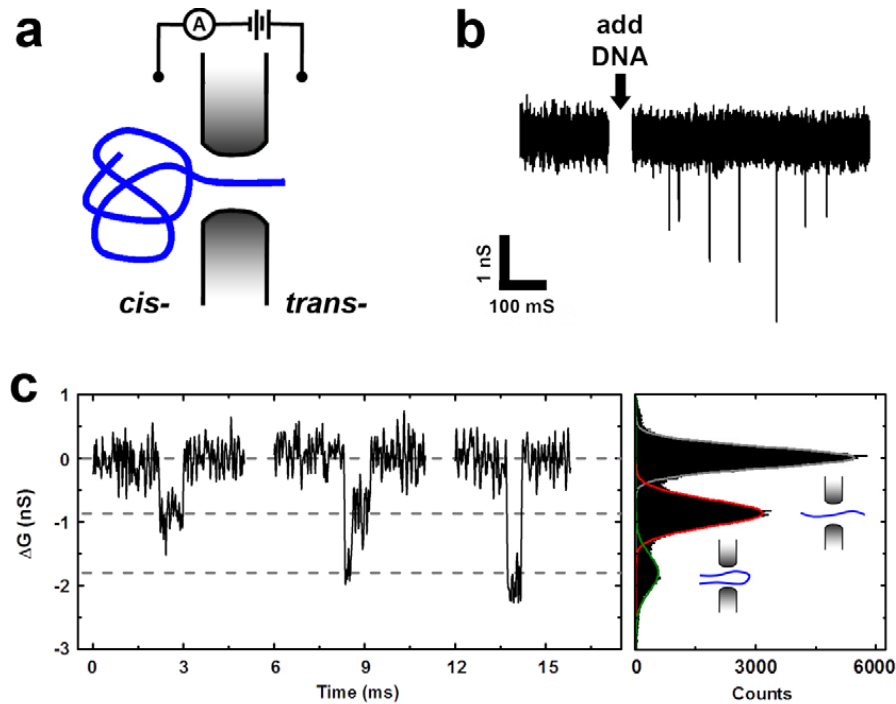


**Figure 1.1. SS-nanopore translocation measurements (5).** (a) Schematic representation of DNA passing through a nanopore. (b) Addition of dsDNA causes intermittent interruptions, or resistive pulses, in the steady baseline current as single molecules transit through the nanopore. (c) Examples of individual events (left panel) containing spatial and temporal information that distinguishes unfolded (left), partially folded (middle), and folded dsDNA (right). Histogram (right panel) of all measured conductance points for 878 individual events.

The spatial parameter of interest is the current change ( $\Delta I$ ) or conductance blockade ( $\Delta G$ ) associated with an event and provides a relative measure of molecular cross-sectional area (Fig. 1.1c) (1). The relevant temporal parameter is event duration ( $\Delta t$ ), which corresponds to the width of the  $\Delta G$  associated with an event and provides a relative measure of a molecule's length and its interactions with the pore. From these data, the structure of biopolymers can be inferred. For example, dsDNA can translocate in either a folded or

unfolded state; folded molecules cause a larger  $\Delta G$ , but transit the pore more quickly, resulting in a shorter  $\Delta t$ . A second important temporal parameter is the number of successive events per unit time, which indicates biomolecule concentration. Together, these three parameters can be used to probe biomolecular characteristics at the single molecule scale in detail and allow SS-nanopores to be employed as a sensitive analytical tool for numerous types of measurements.

For instance, this approach has been used to measure a wide variety of biomolecules (6-8), biomolecular constructs (9,10), and sub-molecular features (11,12), and has recently been applied (13,14) to epigenetic modifications, as well. Early studies using 3 and 10 kilobase (kb) dsDNA were able to distinguish unfolded and folded DNA since translocations of the latter produced multi-level current blockades (6), while later work showed voltage-dependent conductance differences between dsRNA and ssRNA homopolymers (Fig. 1.2) (8). Proteins have been studied less intensively than nucleic acids, but nanopore analyses have revealed several interesting translocation characteristics. For example, proteins tend to translocate much faster than nucleic acids, which are typically much longer, such that temporal resolution limits of the amplifier can hinder accurate measurements and small protein translocations may often go undetected because the signal-to-noise ratio (SNR) is too low (7).

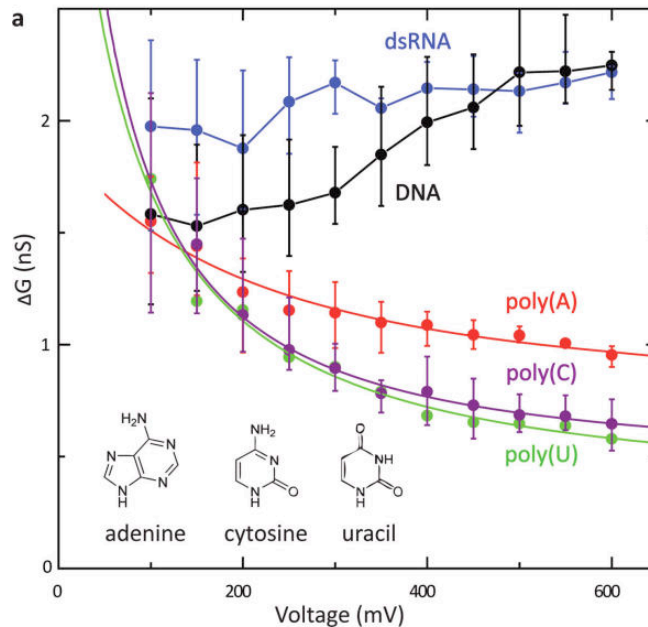


**Figure 1.2. Applied voltage versus mean conductance blockade (8).** Lengths of nucleic acids used in measurements: poly(A) – 10 to 20 kb; poly(U) – 10 to 20 kb; poly(C) – 3 to 10 kb; ds A-RNA – 10 to 30 kb; ds B-DNA – 12.7 kb. At low applied voltage, stretching forces are smaller and homopolymers, which are very flexible, are less extended and occupy larger pore volume. At high voltage, stretching forces are greater, so homopolymers are more extended and occupy smaller pore volume.

Subsequent investigations addressed the potential application of SS-nanopores as sensors of biomolecular complexes. Many DNA-binding proteins play critical roles in biological processes, including transcription, homologous recombination, and packaging chromosomes inside the nucleus (9,10). Using the recombination protein RecA, Smeets *et al.* (2009) found that RecA-DNA complexes produce much larger current blockades than free RecA proteins and showed that comparisons with bare DNA translocations provided accurate size estimates of these nucleoprotein structures. Later work expanded this approach

by measuring RecA-DNA interactions and monitoring current changes to distinguish between protein-coated and uncoated patches, in essence detecting local structure along the length of the DNA-protein construct to generate a topographic map (Fig. 1.3) (9).

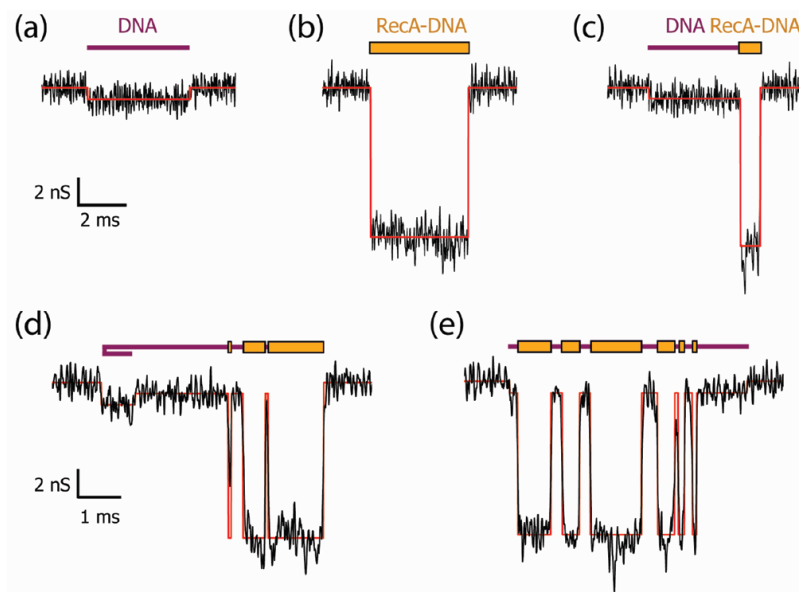


**Figure 1.3. Example SS-nanopore translocation events (9).** Current traces of (a) bare DNA, (b) fully RecA-coated DNA, partially-coated RecA-coated DNA, and (d, e) more complex RecA-coated DNA structures. In cartoon illustrations above traces, DNA is shown in purple and RecA protein in orange.

SS-nanopores have also been used to probe even smaller spatial features created by DNA-intercalating dyes, such as ethidium bromide, propidium, and ethidium homodimer (12). Although these small molecules are only attached to dsDNA between adjacent basepairs, larger current changes were detectable as compared to bare DNA and charge reductions attributable to these dyes increased translocation times (Fig. 1.4). Such high spatial and temporal

resolution may have implications for nanopore-based drug discovery techniques. Similarly, SS-nanopores have been used to sense peptide nucleic acids (PNAs) attached to human immunodeficiency virus (HIV) genes (11). Due to their high sequence-specificity, the PNA oligomer probes bind only to complementary DNA and thus generate a binding pattern, or barcode, that is unique to the target DNA. Such a genotyping approach could lead to nanopore-based pathogen detection systems.

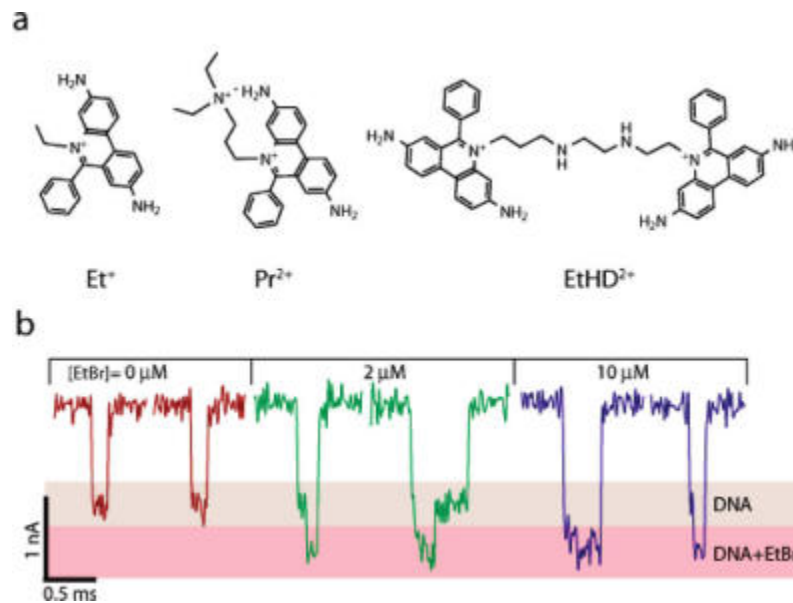


**Figure 1.4. Dye intercalation of dsDNA (12).** (a) Structural formulas for ethidium ( $\text{Et}^+$ ), propidium ( $\text{Pr}^{2+}$ ) and ethidium homodimer ( $\text{EtHD}^{2+}$ ). (b) Example events of 400 bp DNA translocations through a 3.5 nm diameter SS-nanopore at different ethidium bromide (EtBr) concentrations, showing deeper current blockades associated with higher concentrations.

More recently, SS-nanopores have been employed as tools for characterizing epigenetic modifications. Wanunu *et al.* (2011) used small pores 4 nm in diameter to investigate differences between DNA containing cytosine (C-

DNA), methylcytosine (mC-DNA), and hydroxymethylcytosine (hmC-DNA) in DNA and found larger current blockades and longer event durations for hmC-DNA (13). In addition, these differences were influenced in a temperature-dependent manner, indicating thermally activated structural changes that disrupt the hmC-DNA duplex more easily and cause it to be transported through the pore more slowly. Other efforts to accentuate the minor differences between C-DNA and mC-DNA have successfully utilized MBD1 proteins that label methylation sites, resulting in a three-fold increase in the current blockade amplitude over unmethylated DNA (14). Even more recently, SS-nanopores were used to develop a new detection assay that can discriminate between monobiotinylated dsDNA tagged with a streptavidin protein and unmodified dsDNA (Fig. 1.5), demonstrating its efficacy as a highly sensitive diagnostic for epigenetics-level analysis (15).

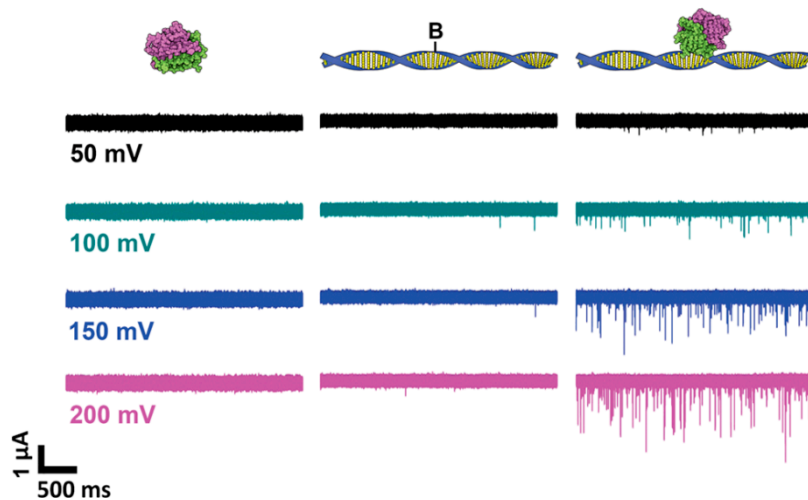


**Figure 1.5. SS-nanopore discrimination of monobiotinylated dsDNA (15).** Monostreptavidin (MS) (left), monobiotinylated 90 bp DNA (bio90) (middle), and MS incubated with bio90 at a molar ratio (MS:bio90) of 8:1 over a range of voltages. Cartoon representations are indicated above each. “B” stands for biotin moiety.

Such advances have continued at a rapid pace since the advent of nanopore research and illustrate the broad utility of single molecule measurements that are label-free and do not rely require sample preparation steps, such as the polymerase chain reaction. These qualities are making SS-nanopores an attractive technology across the “-omics” fields, including genomics, epigenomics (15-19), transcriptomics (20,21), proteomics (22-24), and metabolomics. It also seems likely that system enhancements will ultimately enable SS-nanopores to serve as a next-generation DNA sequencing technology.

#### Conditions to Increase DNA Translocation Times

Smaller molecules have faster translocation speeds than larger ones, but slower events are easier to measure accurately because a longer residence time inside the pore allows more current noise to be filtered out (1). Thus, strategies that can slow down the translocation process are often advantageous, so this subject has been intensively studied. Factors that influence translocation dynamics include both physical and chemical conditions of the measurement system, such as nanopore geometry, electrolyte composition and concentration, pH, and temperature. These considerations are particularly important when the experimental analysis involves very small biomolecules that translocate very quickly since these features may exceed the spatial and/or temporal resolution of the measurement system.

The strength of the electrolyte is important because it affects both the magnitude of the current and translocation speed. First, a larger current results in a larger current blockade during a translocation, thus improving the SNR of the event. Second, application of a voltage across a SS-nanopore exerts a highly localized driving force on charged biomolecules, such as DNA, but this force may be greatly reduced by surface-bound counterions that partially screen DNA's negative charge (25). In addition, more loosely bound, mobile counterions along the surface of the DNA and pore generate an electroosmotic counterflow that further opposes the electrophoretic force experienced by DNA. For potassium chloride (KCl) salt concentrations between 50 mM and 1 M, these effects are relatively constant, so the electrophoretic mobility of DNA, and thus its

translocation time, is constant across this range (26). At KCl concentrations above 1 M, there are only minor increases in translocation times since DNA is already saturated with counterions.

Other salt compositions, however, have been used to further reduce electrophoretic mobility and increase translocation times. As compared to 1 M KCl, measurements using 1 M sodium chloride (NaCl) or lithium chloride (LiCl) salts exhibited longer translocation durations by a factor of 1.7 and 4.8, respectively (Fig. 1.6) (27). Unlike KCl, LiCl concentrations up to 4 M continued to promote even slower translocations.

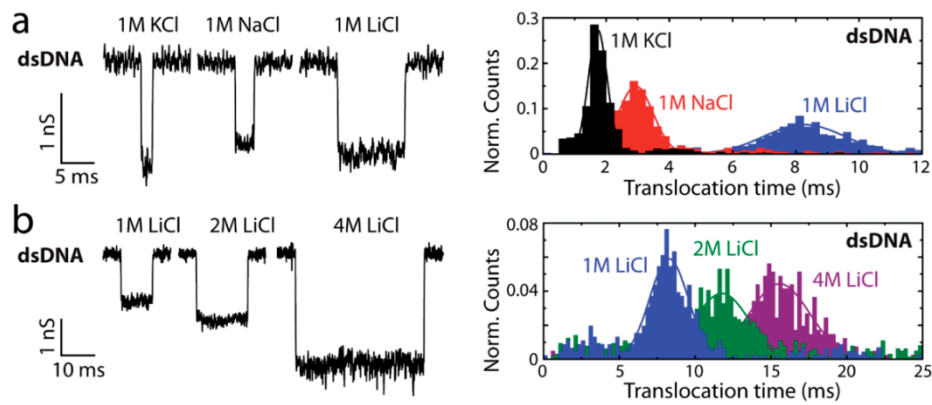


**Figure 1.6. Using salt to slow down DNA translocations (27).** (a) Example conductance traces (upper left) for 48.5 kbp  $\lambda$  DNA at 1 M KCl (left), 1 M NaCl (middle), and 1 M LiCl (right) and corresponding translocation time histograms (upper right). (b) Example conductance traces (lower left) for 48.5 kbp  $\lambda$  DNA at 1 M LiCl (left), 2 M LiCl (middle), and 4 M LiCl (right) and corresponding translocation time histograms (lower right).

Translocation dynamics can also be influenced by introducing asymmetric salt conditions. When a higher concentration is used on the anode side of the pore (opposite the DNA), this sets up a salt gradient that can result in much longer translocation times because cations and anions are affected differently (28). In the case of KCl, for instance, the K<sup>+</sup> ions move down a concentration gradient towards the cathode and also move down an electrical gradient towards the cathode as they are driven away from the anode. In contrast, Cl<sup>-</sup> ions flow down the same concentration gradient, but are pulled in the opposite direction by the electrical gradient. The net effect shifts the voltage drop and focuses more of it outside the pore, thus reducing the electrophoretic force inside the pore.

Both the temperature and pH of the measurement buffer have also been shown to affect translocation speeds. At lower temperatures, less thermal energy is present, resulting in reduced ion mobility and greater solution viscosity (29). A temperature change from 22 °C to 4 °C may produce close to a two-fold increase in DNA translocation times. Variations in pH can be used to generate highly alkaline or acidic conditions, which differ in their effects. Measurements of 3 kbp dsDNA at ~ pH 11.5 demonstrate abrupt decreases in both current blockade and translocation time, attributable to a transition from dsDNA to ssDNA associated with denaturing conditions (Fig. 1.7) (30). In contrast, measurements of 61-bp dsDNA subjected to low pH conditions show increased translocation durations due to acid depurination, which deteriorates the double helical structure and so intensifies interactions with the nanopore (31).

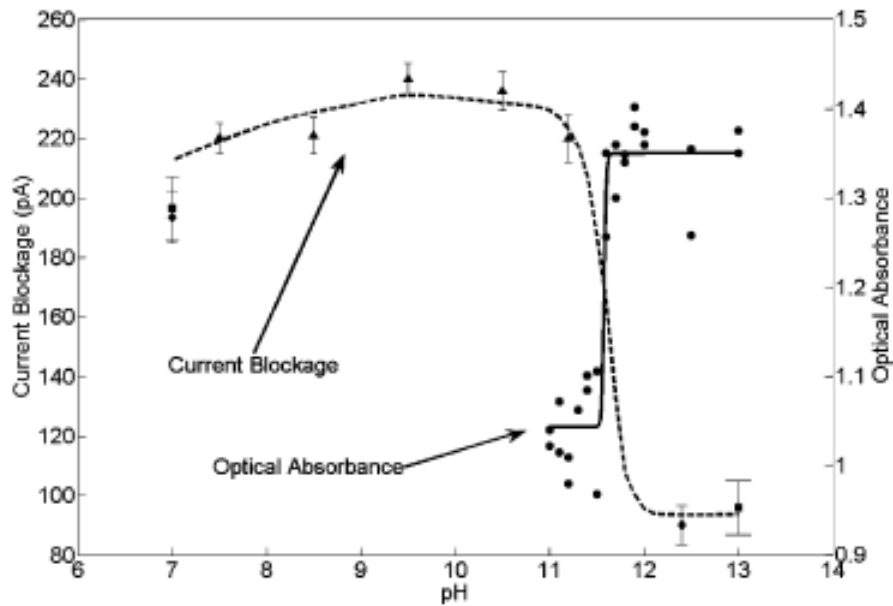


**Figure 1.7. pH versus current blockage for 3 kbp dsDNA (30).** Mean current blockage and DNA optical absorbance as a function of pH. Square, triangle and diamond markers represent different experiments. The dashed line is a guide to the eye.

The physical dimensions of a SS-nanopore are another important source of controlling translocation speeds. A smaller diameter has two primary consequences: first, it promotes unfolded entry of the DNA and more intimate contact with the pore surface, which can enhance electroosmotic effects that oppose the electrophoretic force; second, it also improves the SNR since a larger proportion of the baseline current is blocked. In very small pores  $\leq 4$  nm, DNA can compress the Debye layer, making surface interactions more pronounced and creating an even larger energetic barrier to its translocation (32). A decrease

in pore size from 8 nm to 4 nm can increase the dwell time by almost two orders of magnitude.

The other important aspect of SS-nanopore geometry is membrane thickness. Ion beam milling techniques can be used to controllably remove membrane surface material and decrease this dimension in order to fabricate a thinner membrane. For example, a helium ion beam can be used to thin SiN membranes in a highly controlled, dose-dependent manner (33). Since pores fabricated in thinned membranes are shorter, the pore volume is exponentially smaller than in a larger pore. Since DNA displaces the same volume in both pores, a larger proportion of current is excluded in the smaller pore and results in a larger current blockade. This approach has been used to show that translocations of very small DNA and RNA through ultrathin membranes produce deeper events with much higher SNRs (Fig. 1.8) (34).

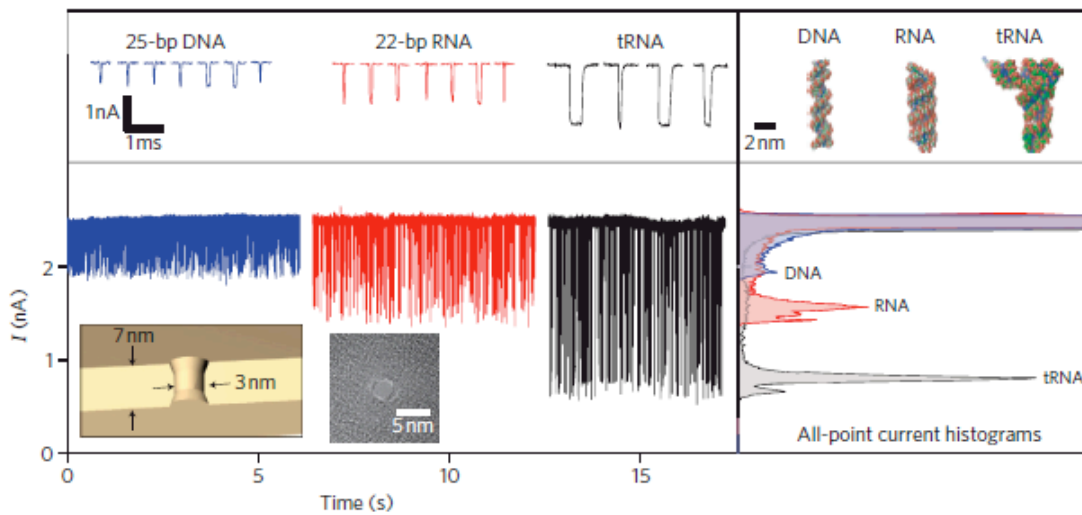


**Figure 1.8. Discriminating small nucleic acids using thin SS-nanopores (34).** Example events (top left) of 25-bp DNA, 22-bp RNA and phenylalanine tRNA with corresponding current versus time traces (below). Models based on crystal structures (top right) and all-point current histograms (below).

## CHAPTER II

### MATERIALS AND METHODS

#### Membrane Thinning Techniques for Nanopore Fabrication

Silicon chips, each supporting a single, freestanding, low-stress SiN membrane, were obtained commercially (Protochips, Raleigh, NC). Atomic force microscopy (AFM) measurements on a broken membrane yielded a film thickness of 105 nm, in agreement with the 100-nm target thickness from the manufacturer. In preparation for fabrication, a single chip was cleaned with acetone followed by ethanol and dried under nitrogen flow. The chip was then loaded into a custom transmission sample holder, the entirety of which was subsequently treated with oxygen plasma (100 W) for 5 min and introduced directly into the sample exchange chamber of a Carl Zeiss Orion Plus Helium Ion Microscope (HIM). Here, an additional treatment of air plasma (10 W, 3 min) was used to ensure minimal contamination of the sample surface before loading the holder into the main chamber of the HIM (Fig. 2.1). In Chapter III, we will discuss a novel method to change membrane thickness that can be implemented at this point in the fabrication process.

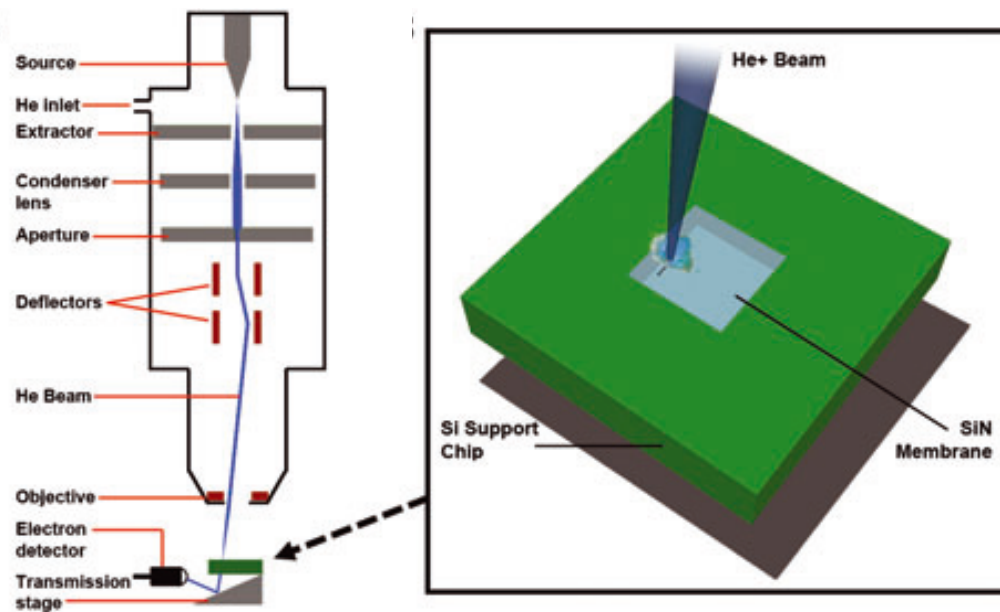


**Figure 2.1. Experimental setup.** Schematic representation of the scanning helium ion microscope demonstrating transmission mode imaging.

### SS-Nanopore Translocation Measurements

Commercial silicon chips, each supporting a free-standing SiN membrane, were purchased from Norcada (Edmonton, Canada) and used as delivered for nanopore fabrication. Membrane thickness was measured to be 24.5 nm using ellipsometry. A single nanopore with a diameter ranging from 5 to 15 nm, depending on the type of measurement, was produced in a membrane using the HIM (Carl Zeiss Orion PLUS, Peabody, MA). In Chapters IV and V, specific diameters are specified for the experimental measurements described there. Pore formation was carried out as reported previously (5).

To prepare the SS-nanopore device for translocation measurements, a chip containing a single SS-nanopore was rinsed with acetone and ethanol, dried under a nitrogen stream, and treated with oxygen plasma (150 W) for 3 min on each side. Immediately after plasma treatment, the chip was seated inside a custom Ultem 1000 flow cell (Fig. 2.2) and wetted by adding 1 M KCl electrolyte.

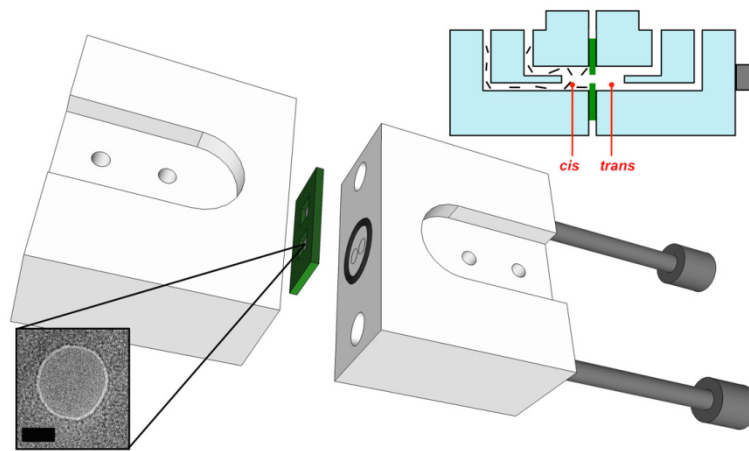


**Figure 2.2. Diagram of SS-nanopore Device.** A chip containing a single nanopore is mounted inside a custom flow cell such that the nanopore is the only connection between each side of the device. An electrolyte is then dispensed into both sides and a voltage difference is applied across the membrane, setting up an electric field inside the nanopore. Lower left inset: transmission electron micrograph of a typical SS-nanopore. Scale bar is 10 nm.

DNA translocations were performed by introducing equilibrated DNA solution into the *cis* flow cell reservoir and applying +200-400 mV to the *trans* chamber using a patch-clamp amplifier (Axopatch 200B, Molecular Devices, Sunnyvale, CA) with a four-pole Bessel filter of 100 kHz. The electrical signal was sampled at 250 kHz and subjected to an additional low-pass filter prior to

analysis using custom LabView software. The specific voltages and filter settings that were used are given in Chapters IV and V.

## CHAPTER III

### MEMBRANE THINNING TECHNIQUES FOR NANOPORE FABRICATION

#### Introduction

The helium ion microscope (HIM) is a promising young technology for high-resolution imaging (35-37). This instrument uses an atomically defined metal source to produce a coherent helium (He) beam with high brightness and small probe size. Through advanced charged particle optics and exploitation of the small de Broglie wavelength of He ions, the HIM is able to achieve a resolution of less than 0.5 nm. Furthermore, due to the slow accumulation of charge caused by the scanning He beam, the HIM has found favor as a means by which to image poorly conducting samples, including uncoated biological material (38,39). Similar to other charged ion beam tools, the HIM can also be used for lithographically defined milling of material. Recent work has shown this capability in various materials including gold (40), graphene (41,42), and silicon nitride (5), demonstrating a high level of control and precision compared to Ga-based focused ion beam (FIB) systems. This stems from the small mass of He relative to Ga, which results in reduced momentum transfer from the ion beam to the target material in the former case and thus a more regulated milling process.

A potential application of this milling control is local thickness manipulation of free-standing membranes. Ion milling is frequently used to create electron-transparent samples for transmission electron microscope imaging (43), but this preparation technique typically only needs to reach thicknesses of approximately 100 nm. Here, deep trenches are milled on either side of a small region of a substrate to achieve a thin cross-section. The HIM provides sufficient control over incident ion dose to reduce self-supported films down to small dimensions through milling in a direction perpendicular to their surface. This capability could have utility in several device architectures in which local thickness is important. For example, solid state nanopores in ultrathin membranes were recently used to detect very short biological molecules with high accuracy (34). Accurate thickness control depends on an elucidation of both direct and transmission milling. In this work, we investigate these aspects of thin film milling experimentally.

### Experimental Methods

Preparation for nanopore fabrication was carried out as described in Chapter II. After loading the prepared chip into the main chamber of the HIM (Fig. 3.1A), the ion beam was unblanked and its current was set to a target value of 5 pA (typical accelerating voltage 30–35 kV) through a 10- $\mu$ m aperture by adjusting the condenser lens setting and the He pressure. Directly prior to milling at the freestanding SiN membrane, beam shape was optimized at a nearby location on the supporting chip. Because the cleaned substrate surface was nominally

featureless, a single-spot exposure (approximately 10 s) with the He beam was used to mill a structure with which to correct focus and stigmatism. Once satisfactorily adjusted, the beam was blanked and the sample was moved such that the SiN window is in the beam path. There, computer control was used to unblank the beam and expose a single square (500 × 500 nm) with a set ion dose (Fig. 3.1B). Direct milling was performed on sample chips with the membrane side up (Fig. 3.1C, top).

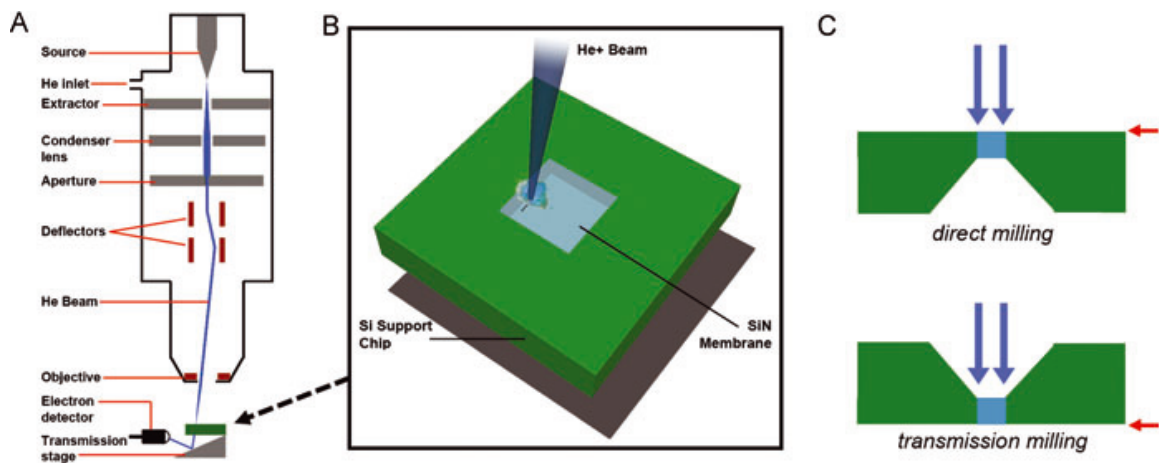


**Figure 3.1. Experimental setup.** (A) Schematic representation of the scanning helium ion microscope, demonstrating transmission mode imaging. (B) Pattern-based helium beam milling of a silicon nitride membrane supported by a silicon chip. (C) Schematic representations of sample chip cross-section for both direct and transmission milling (top and bottom, respectively). Blue arrows indicate milling direction and red arrows indicate the post-processing imaging surface.

Additional squares were milled after moving the membrane a relative lateral distance of 2–4  $\mu\text{m}$  in order to minimize the effects of surface charge

accumulation on the milling process. Completed patterns were inspected *in situ* through transmission imaging (Fig. 3.2A), in which secondary electrons were recorded from an angled metal surface below the thin SiN membrane (see Fig. 3.1A, bottom). The increase in measured brightness at successively higher incident ion dose (Fig. 3.2A, bottom) indicates a greater amount of transmitted ions and thus a thinner remaining membrane thickness within the pattern.

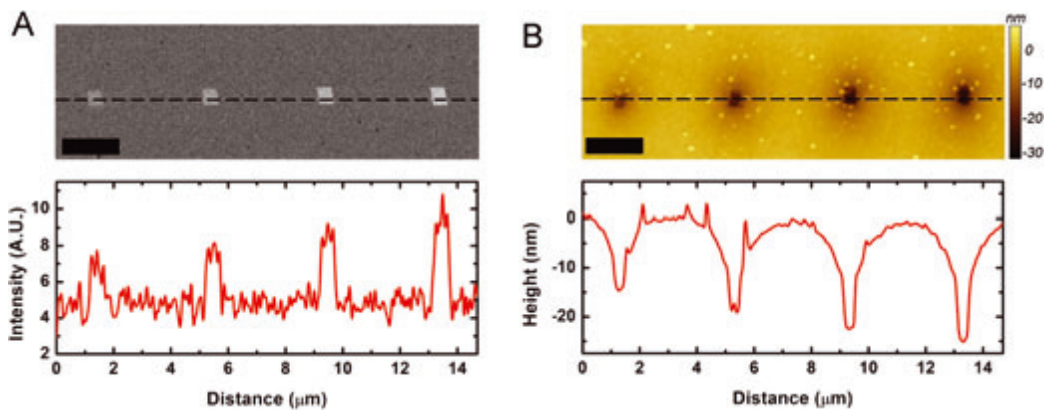


**Figure 3.2. Images of ion-milled patterns.** (A) Transmission HIM image of four helium beam-thinned squares ( $500 \times 500$  nm) in a silicon nitride membrane (top) and brightness profile of the image measured across the dashed line (bottom). (B) AFM image taken on the direct-milling side of the same four squares (top) and the height profile measured across the dashed line (bottom). In both images, the incident ion doses are  $7.6 \times 10^4$ ,  $11.4 \times 10^4$ ,  $13.7 \times 10^4$ , and  $19.3 \times 10^4$  ions/nm<sup>2</sup> (L-R). Scale bars represent  $2 \mu\text{m}$ .

Transmission milling is investigated by mounting a membrane-supporting chip with the membrane side down in the sample holder (Fig. 3.1C, bottom). The same milling procedure as detailed above is performed, resulting in the top (flat)

surface of the substrate being the side opposite to the incident ion beam. This allows for direct access for subsequent AFM imaging.

Following the milling procedure, the sample is removed from the HIM and tapping mode topography images of each milled square are collected using an Agilent 5600LS AFM (Agilent Technologies, Santa Clara, CA). For these images, we use NanoWorld Arrow noncontact tips with a typical radius of curvature of < 10 nm at the tip. The 500-nm width of the square milling patterns allows for the AFM tip to reach the bottom of the trench in all instances.

## Results

A typical AFM image of four squares milled in a SiN membrane is shown in Figure 3.2B. This image is taken from the direct-milling side and shows the same four patterns as in Figure 3.2A. The successively higher incident ion dose from left to right results in increasingly deeper trenches within the confines of the patterns. A topographical measurement across these images (Fig. 3.2B, bottom) confirms this.

The surface contour surrounding the HIM milled patterns on each side is noteworthy. On the direct-milled side, we find a gradual depression beginning 1–2  $\mu\text{m}$  away from the pattern edge (Fig. 3.3A). Meanwhile, on the transmission-milled side, we find a volcano-like structure that surrounds the milled region and gradually declines over a distance of 1–2  $\mu\text{m}$ , with its peak at the pattern edge (Fig. 3.3B). Similarly shaped surfaces have been observed during the closing of prefabricated apertures with a defocused ion beam (44), where the structures

were attributed to accretion of re-deposited matter over long ranges due to electric field effects. This seems to be an unlikely explanation in the present experiments, however, where the additional matter is found only on the transmission side of the membrane. On the side of ion incidence, where the electric field is presumably strongest, we observe the inverse shape. Therefore, we speculate that the topographies of the membrane surfaces surrounding the milling pattern are due to a combination of charge-induced fluidization of the material, as has been documented with an electron beam (45), and ion pressure. A systematic study of these effects may be useful in confirming this assertion. Nonetheless, AFM data of milled membranes and knowledge of the initial membrane thickness allow cross-sectional information to be produced. Figure 3.3C shows three examples of such cross-sections at average doses of (left to right)  $3.9 \times 10^4$ ,  $11.7 \times 10^4$ , and  $19.4 \times 10^4$  ions/nm<sup>2</sup>, respectively. The increasing localized thinning of the membrane with dose is apparent. Interestingly, the lateral size of the exposed area on the transmission side appears slightly smaller than that of the direct side. This may be attributable to complex charging effects, which are difficult to predict.

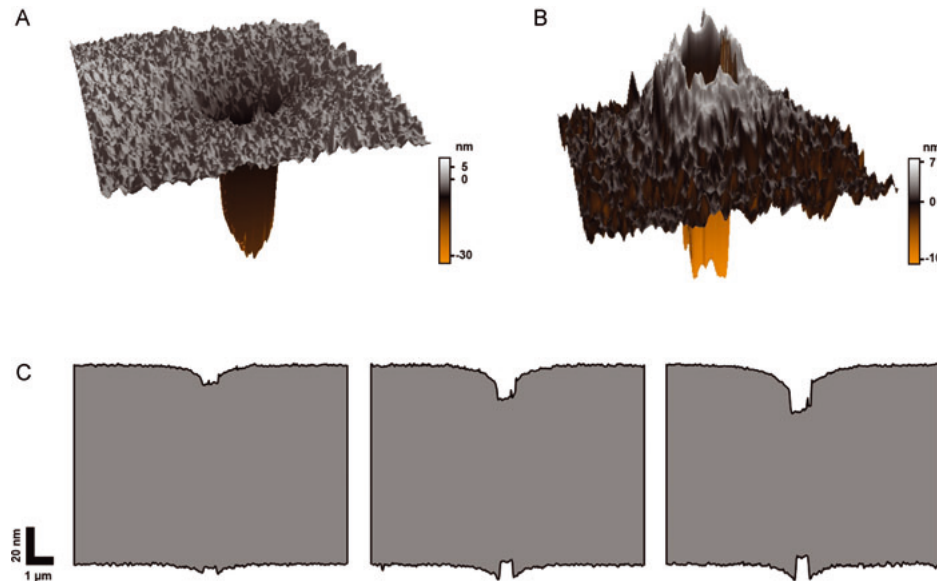


**Figure 3.3. Topographical measurements of direct- and transmission-milled surfaces.** Three-dimensional representation ( $3 \times 3 \mu\text{m}$ ) of AFM topography measurements on the direct- (**A**) and transmission- milled (**B**) side of a SiN membrane. Average He dose is  $19.4 \times 10^4$  ions/ $\text{nm}^2$ . Note that both the direct- and transmission-milled surfaces face upwards for clarity. (**C**) Cross-sectional profiles of SiN membranes with 500-nm squares milled in them, reconstructed from AFM measurements of both the top and bottom surfaces. Doses are  $3.9 \times 10^4$  (left),  $11.7 \times 10^4$  (middle), and  $19.4 \times 10^4$  (right) ions/ $\text{nm}^2$ .

Analysis of milling depth over a range of incident ion doses for the direct-milled side yields a clear linear dependence (Fig. 3.4A). This is in qualitative agreement with experimental (46,47) and theoretical (48,49) findings. A similar analysis of the transmission-milled side yields a dependence that fits well with the square of the ion dose instead (Fig. 3.4B). The shape of this dependence, while qualitatively similar to previous experimental measurements (50) of transmission milling of thin films with ions, is unexpected for our experimental conditions. We discuss this further below.

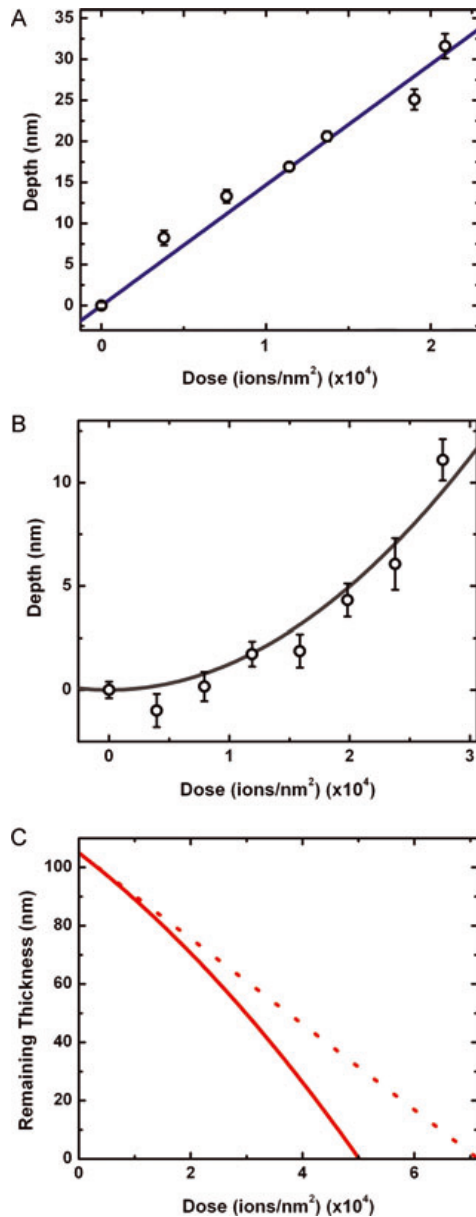


**Figure 3.4. Ion milling depth analysis.** AFM measured depths of direct-milled (A) and transmission-milled (B) squares ( $500 \times 500$  nm) in a 105-nm-thick SiN membrane for different He doses. The blue line in (A) and the gray line in (B) are linear and parabolic fits to the data, respectively. (C) Projected remaining thickness of a 105-nm-thick SiN membrane after exposure to the indicated He ion total dose, based on fits from (A) and (B) (solid line). Dashed line shows remaining thickness based on direct milling only.

## Discussion

On the direct-milling side, our measurements reveal a constant material removal rate of  $1.5 \times 10^{-3} \text{ nm}^3/\text{ion}$ . Using a density of  $3.44 \text{ g/cm}^3$  and a molecular mass of  $140.28 \text{ g/mol}$  for silicon nitride, these data lead to a sputtering yield,  $S$ , of  $0.02 \text{ atoms/ion}$ . For comparison, we performed TRIM calculations (not shown) using values from our system:  $34 \text{ keV}$  He beam energy and  $105\text{-nm}$  SiN membrane thickness. The resultant model yielded a value for  $S$  of  $0.07 \text{ atoms/ion}$ , in reasonable agreement with our experimental findings. Possible contributions to the slight disparity include the effects of local heating and of poor charge dissipation, both of which could impact atomic ejection efficiency but are not accounted for in modeling.

For transmission milling, an explanation for the parabolic dependence of milling depth on ion dose is not readily apparent. The origin of the behavior may be in the continual reduction in membrane thickness during the milling process, as measurements of transmission milling in other films have shown a qualitatively similar increase in yield  $S$  as membrane thickness is reduced (50,51). However, in these cases,  $S$  was shown to decrease for membrane thickness below the mean projected range of the ions. TRIM modeling of SiN (not shown) yields a mean projected range of  $200 \text{ nm}$  for  $34 \text{ keV}$  He ions, indicating that our initial membrane ( $105 \text{ nm}$ ) should already be in the regime where transmission milling yield decreases with reducing thickness. This is counter to our experimental results. It is possible that increasing membrane fluidization lowers the energy

barrier for atoms to be sputtered, but this is difficult to predict and may be expected to be measurable in direct milling as well. A possible explanation for the transmission-milling dependence observed may be direct momentum transfer from nonscattered ions at the transmission surface, the average number of which will increase with reducing membrane thickness. Additional experiments and modeling will be necessary to better understand the overall milling phenomenon in this regime.

With knowledge of the original membrane thickness, the fits to our measurements of direct- and transmission-milled depths amount to a determination of the remaining thickness inside the milled pattern for any given ion dose. Figure 3.4C shows this relation (solid line) in comparison with the remaining thickness dependence if only direct milling is considered (dashed line). The increasing importance of transmission milling at small membrane thickness is evident. Importantly, this assumes constant milling rates down to zero thickness. Considering that ion milling is thought to result from a cascade of atomic interactions within the bulk of the target material (48), this may not be true; as dimensions decrease, there are fewer atoms to interact with one another and thus the rate of milling may be expected to change. This may cause some deviations at very small thickness; however, the delicate nature of such thin free-standing membranes makes AFM measurements challenging. It is unknown where a divergence from the continuous relation shown in Figure 3.4C should be expected, partially because milling in such thin films is not fully understood.

## CHAPTER IV

### DETECTING DNA DEPURINATION

#### Introduction

Depurination is one of the most significant natural mechanisms of DNA degradation, occurring spontaneously under physiological conditions (52). In this process, adenine and guanine bases are liberated when their N-glycosyl linkages to the deoxyribose backbone are hydrolyzed, resulting in an apurinic (AP) site. An estimated 2,000–10,000 purine nucleotides are lost per day in every human cell (53), most often as a result of thermal fluctuations, but potentially also through self-catalyzed mechanisms (54) or through the dissociation of DNA adducts (55). While some AP sites may have functional roles in genetic recombination or nucleosome positioning (54), such lesions generally must be corrected through the base excision repair (BER) pathway (56), creating the potential for elevated mutation rates. As a result, AP sites have been linked to disease initiation, including cancers (55) and anemias (57). A technique capable of linking relative DNA damage with various stages of disease could therefore be potentially transformative for diagnosis and treatment of disorders.

Most conventional methods for detecting AP sites rely on indirect measurement, such as screening for downstream mutations in bacteriophage

(58) or gauging the ability of DNA to act as a template for PCR (59). Recent efforts have also been made to detect by-products of depurination electrochemically (60). More direct methods have been demonstrated as well, utilizing analytical techniques like high performance liquid chromatography (61,62) or colorimetric assays (63). However, these bulk assays are expensive and may mask small but important populations. A rapid technique with single-molecule sensitivity would be of significant value. Recently, An *et al.* (2012) demonstrated the detection of abasic sites using a protein channel (64). This innovative approach has single-molecule sensitivity and can potentially be used to localize AP sites spatially within a known DNA sequence. However, some limitations exist with the technique, related to the chemical labeling method used, the reliance on a fragile lipid membrane, and importantly, the inability to investigate double-strand (ds) DNA.

In this report, we demonstrate a new assay for the detection of depurination in short duplex DNA using solid-state (SS-) nanopores. SS-nanopores are an emerging technique (1,65,66) in which individual molecules are threaded electrokinetically through a narrow aperture fabricated in a thin, solid-state membrane. As they translocate, their characteristics can be determined through resistive pulse sensing (Fig. 4.1a). This approach has been used to measure a wide variety of biomolecules (6-8), biomolecular constructs (9,10), and sub-molecular features (11,12), and has recently been applied (13,14) to epigenetic modifications, as well.

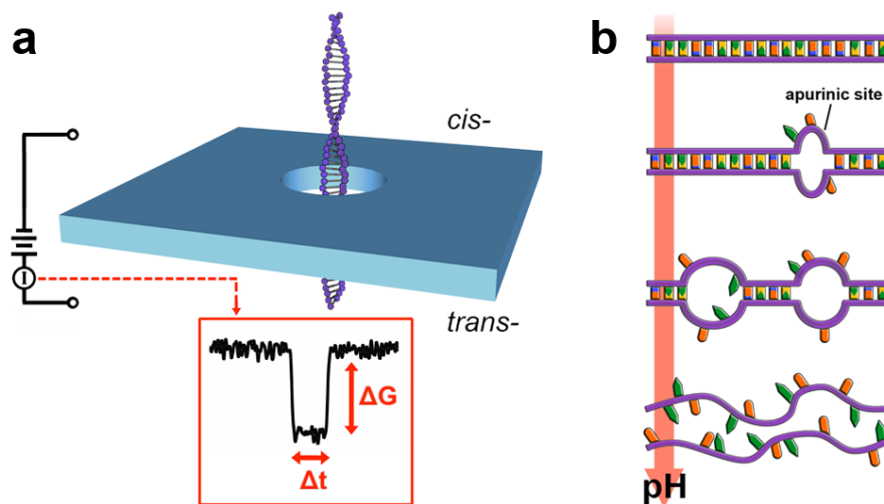


**Figure 4.1. SS-nanopore detection of DNA depurination.** (a) Schematic of the measurement system. A voltage applied across a membrane containing a single nanopore drives dsDNA from the *cis*- side to the *trans*- side. Inset: typical conductance blockade event shape with depth ( $\Delta G$ ) and duration ( $\Delta t$ ) indicated. (b) Cartoon representation of pH-induced DNA depurination. Acidic conditions preferentially remove purine bases (G and A), causing a progressive loss of structure.

Here, we apply SS-nanopores to study unlabeled, heteropolymeric dsDNA and investigate the translocation dynamics of this model molecule with varying amounts of depurination induced through acid hydrolysis. We show that AP sites produce translocation durations that are up to an order of magnitude greater than what is measured for untreated material. The level of depurination can be coarsely estimated for each individual molecule as it translocates and bulk depurination levels can be assessed from a series of single-molecule measurements. As a result, our technique has potential as a sensitive, label-free diagnostic of AP site density in DNA.

Experimental methods to induce depurination in DNA have become well-established, given its fundamental significance. Both heat and chemical treatments (e.g. ethyl ethane sulfonate) are effective depurinating agents that remove guanine preferentially from DNA (58,67). However, solvent chemistry and temperature may affect SS-nanopore translocations independently, and so we instead vary the density of AP sites using pH (Fig. 4.1b). Acidic conditions are known to protonate DNA and hydrolyze purine residues, so pH is used commonly to induce depurination in biochemical assays like Southern blotting (68). Therefore, through measurements across a broad pH, we are able to investigate the effects of substantial differences in the amount of depurination.

In order to probe these effects systematically, we use a series of SS-nanopores (four separate devices) ranging in diameter from 5–6 nm to translocate 61 bp DNA in high-ionic strength measurement solution (1 M KCl) over a pH range from 2 to 10. In each case, the duplex DNA is incubated at a given pH for 1 hr before being introduced to the grounded *cis* side of a pore (Fig. 4.1a). The application of a positive voltage (400 mV) to the *trans* side is then used to induce translocations. Threading of molecules through the SS-nanopore is manifested by brief, transient blockade events (Fig. 4.1a, inset) in the measured trans-pore ionic conductance that are described by a characteristic depth ( $\Delta G$ ) and duration ( $\Delta t$ ). We record a constant succession of blockade events under all investigated conditions.

### Experimental Methods

Duplex 61-mer DNA with a sequence of 5'-  
TACTGCTAGCAATGCCCTGGAACGGAATTCTTAATAAAGATGTATCATTCTG  
CAGTACT- 3' was purchased from Integrated DNA Technologies (Coralville, IA),  
re-suspended at a concentration of 4 mg/ml in 10 mM Tris buffer, 1 mM EDTA  
(pH 8), and stored at -20°C. Each pH treatment was prepared by adding (at a  
1:100 ratio) this stock DNA to 1 M KCl measurement solution at the desired pH  
and incubating the mixture at room temperature for 1 hour. Solution pH was  
adjusted by adding sodium carbonate/bicarbonate (pH 10), Tris (pH 8), sodium  
acetate (pH 6), sodium citrate (pH 4), or HCl (pH 2).

Nanopore fabrication and preparation for experimental translocations were  
performed as described in Chapter II, except as noted here. In these  
experiments, nanopores with diameters of 5–6 nm were used. After nanopore  
preparation, it was placed in high humidity to reduce evaporation and left at room  
temperature to equilibrate for the same one-hour DNA incubation period. For the  
additional pH 4 treatment, the pore was equilibrated in 1 M KCl at pH 8.

DNA translocations were performed by introducing equilibrated DNA  
solution (at a concentration of ~ 40 ng/μl) into the *cis* flow cell reservoir and  
applying +400 mV to the *trans* chamber using a patch-clamp amplifier (Axopatch  
200B, Molecular Devices, Sunnyvale, CA) with a four-pole Bessel filter of 100  
kHz. The electrical signal was sampled at 250 kHz and subjected to an additional  
low-pass filter of 50 kHz prior to analysis using custom LabView software. The

total numbers of events considered were as follows:  $n = 714$  (pH 10), 662 (pH 8), 552 (pH 6), 423 (pH 4) and 1852 (pH 2).

The gel electrophoresis assay was performed using equal amounts of 61 bp dsDNA in each lane. For this measurement, dsDNA was incubated for 1 hr at a given pH as described above and then loaded directly onto a 1% agarose gel prepared with a Tris/Borate/EDTA buffer solution (pH 8.3) and an intercalating dye (Ethidium Bromide Solution, Promega Biosciences, San Luis Obispo, CA).

### Results and Discussion

As pH is reduced, we find only negligible changes in the depth of measured events, yielding a mean  $\Delta G$  of 1 nS (Fig. 4.2). This value agrees with numerous other reports of dsDNA translocations under comparable high-ionic strength conditions (4,6,8) and is consistent with simple size-exclusion (26). Importantly, however, we find that translocation duration changes considerably over the same pH range. Under all measured levels of pH (Fig. 4.3a & b), we observe a significant population of events with a mean  $\Delta t$  of  $\sim 70\text{-}100 \mu\text{s}$ . We attribute this consistent duration to the passage of native, non-degraded dsDNA, which should be present to some degree under all conditions.

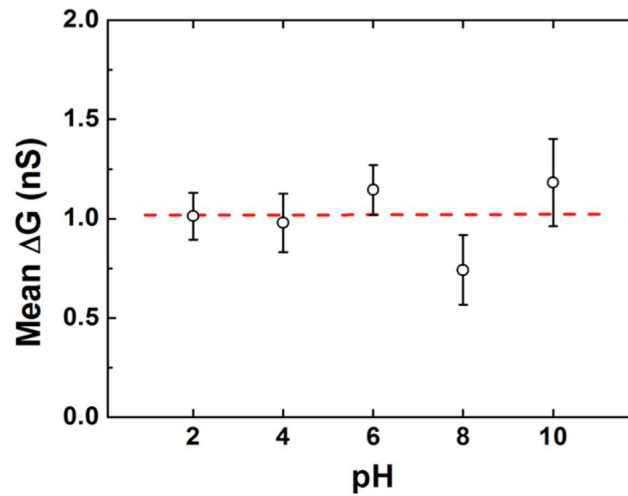


**Figure 4.2. Conductance blockade depth across the pH range.** Mean conductance change measured for 61 bp DNA translocations from pH 2-10. No significant variation is observed. Error bars represent the width of a Gaussian fit to the data and the dashed line represents the average value from all data sets.

However, at low pH ( $\leq 6$ ), an additional population emerges with much longer duration. We note that a small number of slow events ( $\sim 200 \mu\text{s}$ ) is also observed at pH 8, but these events are rare and thus cannot be adequately fitted with a Gaussian distribution. At pH 6, we find a population with a mean  $\Delta t$  of  $280 \mu\text{s}$ ; at pH 4, a mean  $\Delta t$  of  $610 \mu\text{s}$ ; and at pH 2, a mean  $\Delta t$  of  $1140 \mu\text{s}$ , an order of magnitude greater than the unmodified duration. We suggest that the longer translocation times occur because the native DNA helix is disrupted as purines are liberated at low pH, resulting in unstructured regions characterized by missing base-pairs and strand separation. Both of these consequences may contribute to greater interaction with the pore walls and thus slower translocation times. First, unpaired nucleotides opposite abasic sites can rotate more freely

and interact directly with the pore. Second, separated strands occupy a larger effective volume, potentially increasing the amount of time the DNA is in contact with the pore. Under extreme conditions of pH, the exposed phosphodiester backbone and increased inter-molecular coupling can facilitate complex configurations that are often unable to pass through the pore. Indeed, for many devices, we observe irreversible clogging of the pore at pH 2 (data not shown), which we attribute to attempted threading of DNA with extensive structural damage.

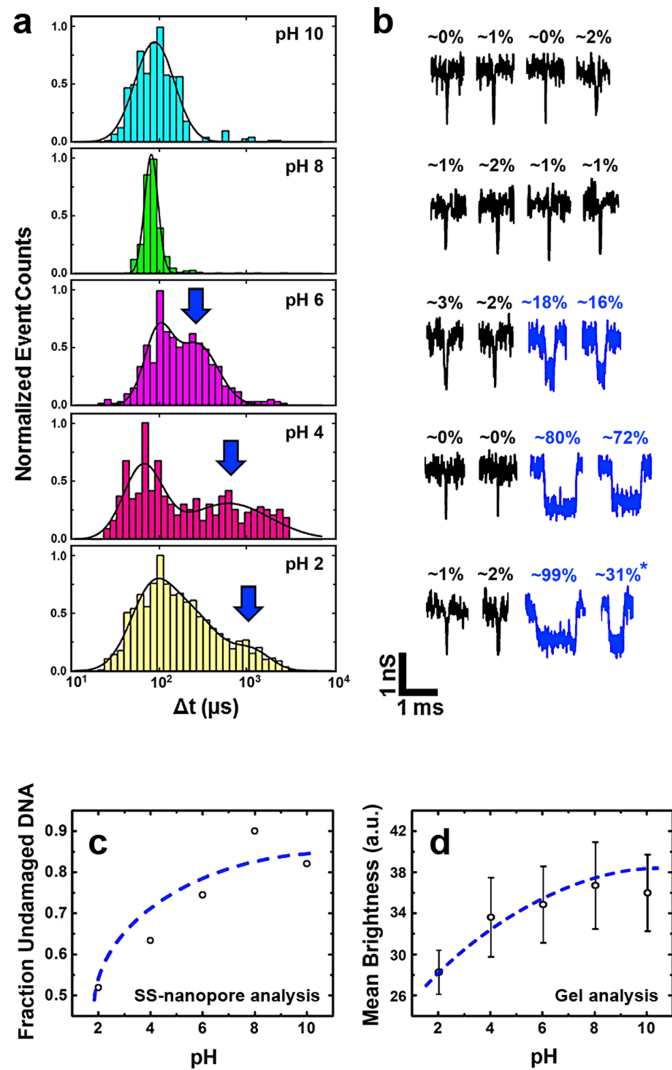


**Figure 4.3. pH effects on 61 bp DNA.** (a) Event duration histograms for translocation measurements from pH 10 (top) to pH 2 (bottom). Total numbers of events are:  $n = 714$  (pH 10), 662 (pH 8), 552 (pH 6), 423 (pH 4) and 1852 (pH 2). Black lines represent Gaussian fits to the data. (b) Example traces of typical events measured at each pH level. Black traces represent undamaged (low  $\Delta t$ ) events. Blue traces (pH 6, 4 and 2) represent damaged (i.e. depurinated) events derived from the high  $\Delta t$  population, indicated by blue arrows on the histograms. Event trace labels indicate coarse approximations of the relative amounts of depurination. The final event at pH 2 (marked with \*) may indicate DNA fragmentation. (c) Fraction of translocation events in the undamaged population. (d) Intensity of DNA bands on a gel, measured over the entire range of pH investigated. Dashed lines are logarithmic fits to the data.

We note that the data taken at pH 2 yields a large number of events with durations intermediate to the two dominant populations (see Fig. 4.3a, bottom). We attribute these to a complete loss of duplex structure into single-stranded DNA polymers and possible fragmentation, which is known to occur at higher rates under acidic conditions (69). Translocation of these smaller molecules will have the effect of reducing the measured  $\Delta t$  from the depurinated level. We also note that there is some variation in the distribution widths of the fast translocation (70-100  $\mu$ s) population between various pH levels, with the narrowest distribution occurring at pH 8. We suggest that this is because the dsDNA is most structurally stable under this near-physiological condition; at pH 10, for example, electrostatic repulsion of the backbones can cause localized denaturation and thereby produce variation in event dwell time.

We find that a decreasing proportion of recorded events falls inside the limits of the undamaged population as solvent conditions are made more acidic (Fig. 4.3c). This is in accordance with expectations, considering that the level of DNA depurination is known to increase rapidly as pH is reduced (53). We also investigate the same molecules treated at each pH by gel electrophoresis (Fig. 4.4). Since dye intercalation will be hindered by loss of helical structure, we anticipate that the amount of DNA that can be visualized on such a gel will be reduced as depurination density increases. Analysis of band intensity confirms this (Fig. 4.3d), yielding a qualitatively similar logarithmic dependence on pH. This is a reasonable relation considering that pH is a logarithmic measure of

solution hydronium ion content. This result provides secondary confirmation of our approach.

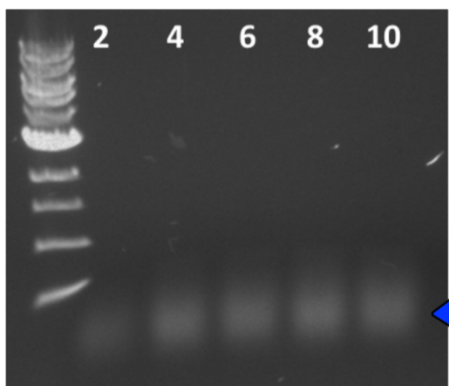


**Figure 4.4. Gel analysis of DNA across a pH range.** Gel electrophoresis performed on 61 bp DNA subjected to various pH conditions, indicated at the top of each lane. The blue arrow indicates the position of 61 bp DNA.

Importantly, due to the nature of SS-nanopore measurements,  $\Delta t$  can be assessed for individual events, providing a rough estimate of the relative density of AP sites present in each molecule. Fig. 4.3b shows example traces of dsDNA events with low (black) and high (blue, where applicable)  $\Delta t$  for each pH level investigated. If we assume that the minimum duration ( $\sim 80 \mu\text{s}$ ) represents undamaged dsDNA and that the maximum duration observed ( $\sim 1 \text{ ms}$ ) represents DNA that is almost completely depurinated, then the relative level of depurination for all intermediate events can be approximated by event  $\Delta t$  (see Fig. 4.3b). While we stress that this estimation is coarse, we find mean depurination levels of  $\sim 21\%$  at pH 6 and  $\sim 58\%$  at pH 4.

A possible alternative explanation for the observed differences in event duration could be changes in the net electrical forces at play in the SS-nanopore caused by protonation. Firnkes *et al.* (70) demonstrated that the electrophoretic and electroosmotic forces acting on proteins could be modified or even reversed due to pH-induced surface charge effects in a comparable system. However, these measurements were performed in low ionic strength solution. The extent to which pH can alter translocation dynamics depends, in part, on the relative zeta potentials of the nanopore and analyte. Since Manning condensation (71) reaches saturation in high ionic strength solvents, charged surfaces are better shielded and zeta potential changes are inhibited under these conditions. As a result, electrophoretic forces are expected to remain relatively constant over a wide range of pH and electroosmotic flow inside the nanopore is suppressed. Indeed, recent work by Anderson, *et al.* (72) showed that the translocation dynamics of dsDNA in 1 M KCl were insensitive to pH unless the SS-nanopore was functionalized with an organic coating.

In order to isolate effects of dsDNA structural changes (i.e. depurination) from these purely electrical effects, we perform an additional experiment in which we first incubate 61 bp DNA in 1 M KCl at pH 4 as above, but subsequently adjust the solution to 1 M KCl, pH 8 prior to SS-nanopore measurement. In this way, the irreversible structural modifications can be investigated under the same translocation conditions that yield a single, well-defined  $\Delta t$  population when untreated dsDNA is measured (see Fig. 4.3a). This allows any pH-induced

counterion effects (such as electroosmosis) to be separated from the depurination process itself.

As shown in Fig. 4.5, these measurements yield a  $\Delta t$  histogram similar to that of translocations performed using pH 4 measurement solution, with a significant peak around 68–95  $\mu\text{s}$  and a large population of events extending to longer durations. The locations of the long  $\Delta t$  population under both conditions are within error of each other. These translocation results support our hypothesis that the increased  $\Delta t$  we observe using a SS-nanopore analysis of low-pH events is caused by depurination-induced changes in the DNA structure.

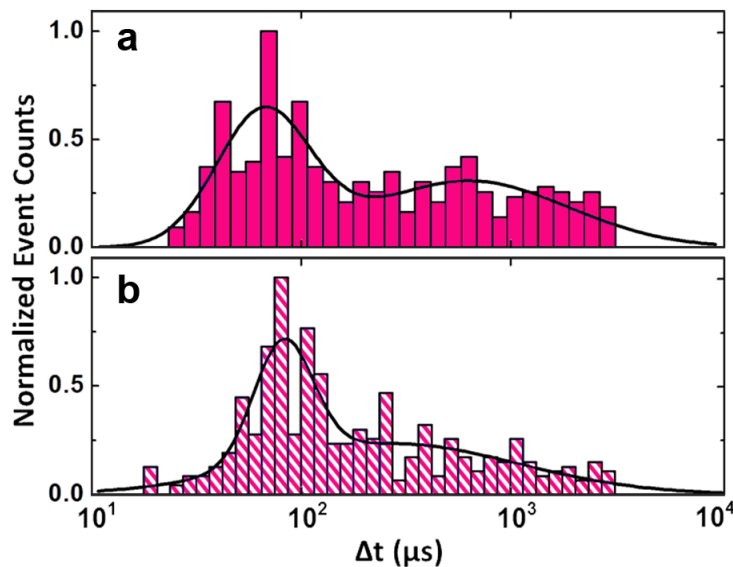


**Figure 4.5. Isolating structural factors from solvent effects.** Dwell time histograms for two different SS-nanopore measurements of dsDNA incubated at pH 4. (a) Incubation and measurement in 1 M KCl at pH 4 (same data as pH 4 histogram in Fig. 4.3) and (b) incubation in 1 M KCl at pH 4 and measurement in 1 M KCl at pH 8 ( $n = 408$ ).

## CHAPTER V

### USING SINGLE-STRANDED BINDING PROTEINS TO DIFFERENTIATE DOUBLE- AND SINGLE-STRANDED DNA

#### Introduction

Solid-state nanopores (SS-nanopores) are part of a new and promising class of analytical platforms for characterizing biomolecules at the single molecule scale. They offer a level of sensitivity that enables a much wider range of biochemical investigations than was possible even a few years ago. Several studies have demonstrated the wide-ranging potential of SS-nanopores as single molecule sensors capable of distinguishing ds- and ssDNA. Electrical signals associated with RNA homopolymers of poly(A), poly(C), and poly(U) differ from each other and from dsRNA and dsDNA molecules (8). Heteropolymeric dsDNA polymers exhibit large current blockades and dwell times that differ from their denatured single-stranded counterparts when translocations are measured under alkaline pH conditions (30). Distinct differences are also apparent at neutral pH, where heteropolymeric ssDNA self-hybridizes into more complicated secondary structures that produce much larger current changes than dsDNA of the same length (73). In another approach, small SS-nanopores (~ 4.5 nm in diameter) have been used to prevent the entry of folded ssDNA, thus resulting in much faster translocations than for dsDNA of comparable size (74).

Another class of SS-nanopore experiments show marked changes in the electrokinetic behavior of DNA when various proteins are used as binding agents. In the first nanopore measurements of DNA-protein complexes, translocations of dsDNA coated with recombination protein A (RecA) resulted in much larger conductance blockades than either dsDNA or RecA by itself (10). Subsequent work demonstrated that conductance signatures could also be resolved for RecA-coated patches of local structure within a single DNA molecule (9). Additional measurements have also shown characteristic differences between histone substructures (75) as well as differences between native and streptavidin-tagged dsDNA (15). Such results emphasize the importance of additive effects in single molecule measurements, where a small difference in size and/or charge can render certain analytes virtually undetectable.

In this work, we describe an approach in which the *E. coli* single-stranded DNA-binding protein (SSB) is employed as a biomolecular tool to differentiate double-stranded (ds) and single-stranded (ss) DNA. Believed to be an essential protein in all organisms, SSB is critically important in many cellular processes, participating in DNA recombination, repair, and replication (76,77). Its capacity for binding with high affinity to ssDNA in a cooperative manner is intrinsic to each of these functions.

Since it binds preferentially to ssDNA, SSB could be a useful screening agent in many assays where electrokinetic differences from dsDNA are important. In our approach, we use SS-nanopores ~ 12 nm in diameter to

measure the translocation behavior of the ssDNA-SSB complex (Fig. 5.1a). Application of a voltage across the SS-nanopore generates an electric field that results in a stable ionic current through the pore. Upon introduction of these nucleoproteins, we find pronounced changes in the trans-pore current associated with individual translocations, which we quantify in terms of mean conductance blockade ( $\Delta G$ ) and translocation duration ( $\Delta t$ ) (Fig. 5.1b).

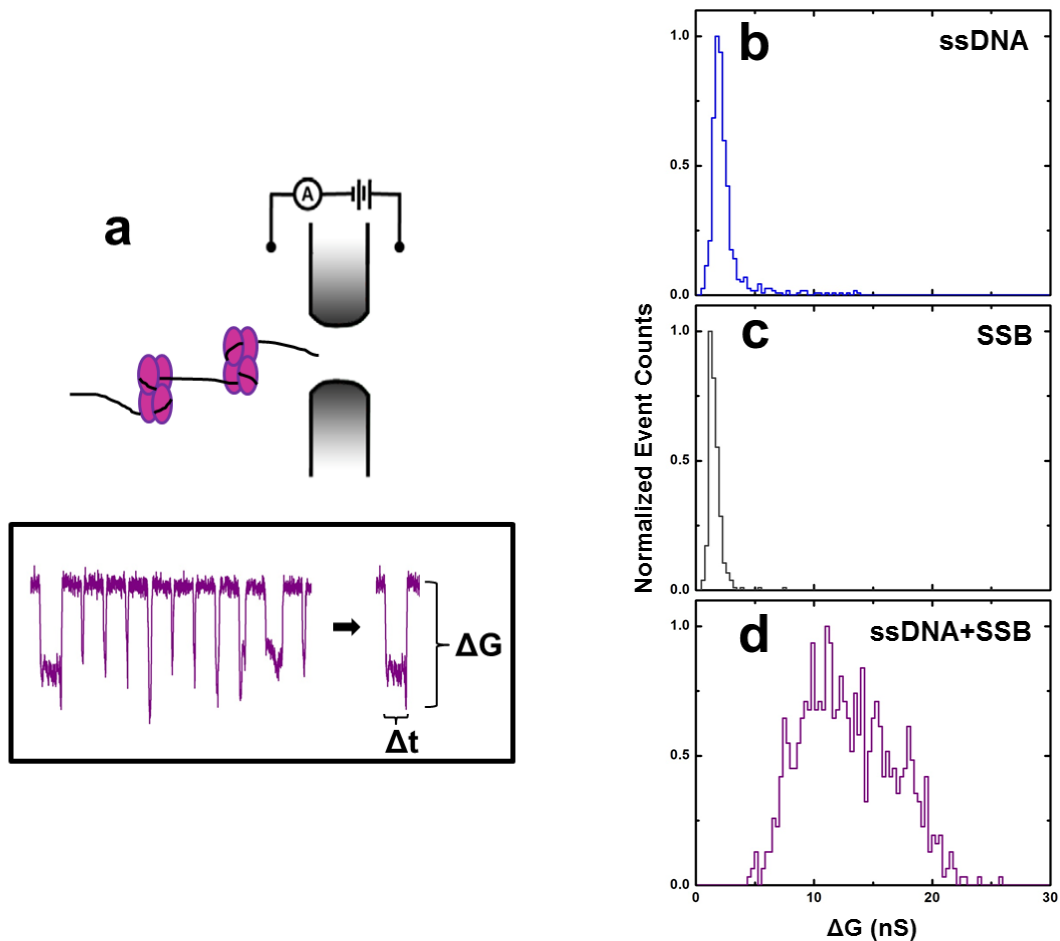


**Figure 5.1. SS-nanopore detection of the DNA-SSB complex.** (a) Schematic of the measurement system. Application of a voltage across the membrane pulls SSB-bound ssDNA through the nanopore from the *cis*- side to *trans*- side. Inset: example trace of translocation conductance blockades and typical event with depth ( $\Delta G$ ) and duration ( $\Delta t$ ) indicated. (b)  $\Delta G$  histograms of ssDNA (2.5 ng/ $\mu$ l,  $n = 551$ ), SSB (224 ng/ $\mu$ l,  $n = 327$ ), and ssDNA (2.5 ng/ $\mu$ l) incubated with SSB (22.4 ng/ $\mu$ l) at a molar ratio of (ssDNA:SSB) of 1:284 ( $n = 824$ ). Binding of SSB to ssDNA causes a pronounced shift in the mean  $\Delta G$ .

### Experimental Methods

M13mp18 Single-stranded DNA (circular ssM13) (7249 b, 250  $\mu$ g/ml),  
M13mp18 RF I DNA (dsM13) (7249 bp, 100  $\mu$ g/ml), and *Bam*HI (20,000

units/ml) were purchased from New England BioLabs (Ipswich, MA) and stored at  $-20^{\circ}\text{C}$  upon arrival until use. A 25-base DNA oligonucleotide (25-mer) with sequence 5'- ACCGAGCTCGAATTCGTAATCATGG-3' complementary to circular ssM13 was purchased from Integrated DNA Technologies (Coralville, IA), re-suspended at a concentration of 4 mg/ml in 10 mM Tris buffer, 1 mM EDTA (pH 8), and stored at  $-20^{\circ}\text{C}$ . Single-strand Binding Protein from *Escherichia coli* (4470  $\mu\text{g/ml}$ ) was purchased from Sigma-Aldrich (St. Louis, MO) and stored at  $-20^{\circ}\text{C}$  upon arrival until use.

DNA and SSB were prepared for individual measurements by adding stock solutions to 1 M KCl (pH 8) at a 1:100 ratio. For the titration series measurements, DNA-SSB reactions were prepared by adding to 1 M KCl (pH 8) DNA stock solution at a 1:100 ratio and SSB stock solution at the following ratios: 1:2000, 1:500, 1:286, 1:200, and 1:20. Reaction mixtures were left overnight at room temperature prior to measurement.

Linear M13 ssDNA was prepared by enzymatic digestion of a dsDNA *Bam*HI restriction site that was generated by annealing the 25-mer to the circular ssM13. Typically, the circular ssM13 (20 nM final concentration) and 25-mer (160 nM final concentration) were combined to prepare a hybridization reaction and heated at  $95^{\circ}\text{C}$  for 3 min., cooled to room temperature over 30 min., and stored at  $4^{\circ}\text{C}$ . Restriction digestions were prepared using 10  $\mu\text{l}$  of hybridization reaction, 20 U of *Bam*HI (1  $\mu\text{l}$ ), and 4  $\mu\text{l}$  of 1X CutSmart Buffer for a final volume of 15  $\mu\text{l}$  and incubated at  $37^{\circ}\text{C}$  for 1.5 hr. The reaction product was loaded onto

a 0.8% agarose gel and the resulting band was excised and then purified using a Promega Wizard SV Gel and PCR Clean-Up System Kit. After eluting the final product with nuclease-free water, its concentration was measured using a Nanodrop 2000c Spectrophotometer.

Nanopore fabrication and preparation for experimental translocations were performed as described in Chapter II, except as noted here. In these experiments, nanopores with diameters of 11–13 nm were used. DNA translocations were performed by introducing DNA (at a concentration of ~ 2.5 ng/ $\mu$ l) or SSB solution (at concentrations ranging from ~ 2.2 to 224 ng/ $\mu$ l) into the *cis* flow cell reservoir and applying +200 mV to the *trans* chamber using a patch-clamp amplifier (Axopatch 200B, Molecular Devices, Sunnyvale, CA) with a four-pole Bessel filter of 100 kHz. The electrical signal was sampled at 250 kHz and subjected to an additional low-pass filter of 30 kHz prior to analysis using custom LabView software.

In the gel electrophoresis assay comparing different ratios of DNA:SSB, equal amounts of DNA (~ 25 ng) were used in each lane, while varying the amounts of SSB according to the ratios noted for the titration series measurements above. For this measurement, DNA-SSB reactions were incubated overnight at room temperature and then loaded directly onto a 1% agarose gel prepared with a Tris/Borate/EDTA buffer solution (pH 8.3) and an intercalating dye (Ethidium Bromide Solution, Promega Biosciences, San Luis Obispo, CA). In the gel assay comparing circular ssM13, linearized ssM13, and

double-stranded DNA, equal amounts of DNA were used (~ 25 ng), except for the linearized ssM13 (~ 4 ng). For this measurement, DNA solutions were prepared and then loaded directly onto a 1% agarose gel prepared with a Tris/Borate/EDTA buffer solution (pH 8.3) and an intercalating dye (Ethidium Bromide Solution, Promega Biosciences, San Luis Obispo, CA). To visualize ssDNA, the gel was also incubated in Diamond™ Nucleic Acid Dye (Promega Biosciences, San Luis Obispo, CA).

### Results and Discussion

In solution, SSB assembles into a stable homotetramer with a molecular weight of 74 kDa and a Stokes radius of ~ 4 nm (76). The isoelectric point (PI) of SSB is 6.0 (77-79), so it has a negative charge at pH 8, the measurement conditions used here. Except for the final experiment (discussed below), our binding assays utilize a circular form of ssDNA, which occurs naturally in M13mp18 filamentous bacteriophage and is readily available commercially. Only minor differences are apparent in a comparison of ssDNA and SSB conductance blockade histograms (Fig. 5.1b, c), which show a mean  $\Delta G$  of  $2.1 \pm 0.5$  nS and  $1.6 \pm 0.4$  nS, respectively. This is consistent with previous work, which typically finds that free protein translocations are rapid with small  $\Delta G$  signatures (70,80). A previous report (73) found deep (> 10 nS) events exclusively for ssDNA under comparable solvent conditions. While we do observe some deep events here, they are instead a minor population within the results. We attribute this to the larger SS-nanopore size used in our experiments; indeed, measurements using a

6 nm nanopore are very similar to previous work, resulting in a mean  $\Delta G$  of  $9.7 \pm 1.7$  nS.

Translocations of the DNA-SSB complex (Fig. 5.1d), however, exhibit a much larger mean  $\Delta G$  of  $12.7 \pm 4.4$  nS, indicating structural alterations that cause significant electrokinetic changes. An important parameter that governs SSB binding is the number of nucleotides ( $n$ ) occluded by the protein when bound, or its site size  $(SSB)_n$ , which is important for obtaining both structural and quantitative information (77). This value depends on salt concentration, in part, and experimental evidence suggests that three different binding modes are possible:  $(SSB)_{35}$  in which two SSB subunits are bound at low salt ( $\leq 10$  mM),  $(SSB)_{56}$  in which the other two subunits become involved between 10 and 200 mM, and  $(SSB)_{65}$  in which all four subunits are stably bound at high salt ( $\geq 200$  mM). The molecular differences between  $(SSB)_{56}$  and  $(SSB)_{65}$  are unknown, although it has been suggested that  $(SSB)_{65}$  also favors a periodic grouping of bound tetramers to form higher-order structures (77). Thus, the DNA-SSB complex would be expected to assume the  $(SSB)_{65}$  configuration at 1 M KCl, as used here.

Nanopore measurements of SSB mixed with a 61 base DNA oligonucleotide in 1 M KCl result in only minor differences (Fig. 5.2), possibly due to little or no bound SSB since the DNA binding length is less than 65 nucleotides. Results of an electrophoretic mobility shift assay (EMSA), however, more clearly indicate that a complex is formed after incubating the

oligonucleotide with SSB (Fig. 5.3). This difference may be attributable to a lower final salt concentration of  $\sim 500$  mM KCl due to the addition of loading dye to these mixtures. Although this is still above the 200 mM threshold where  $(\text{SSB})_{65}$  binding mode interactions are expected, these results suggest that this may be a transitional salt regime that also supports the formation of  $(\text{SSB})_{56}$  complexes in which 61 b DNA would provide a sufficient binding length.

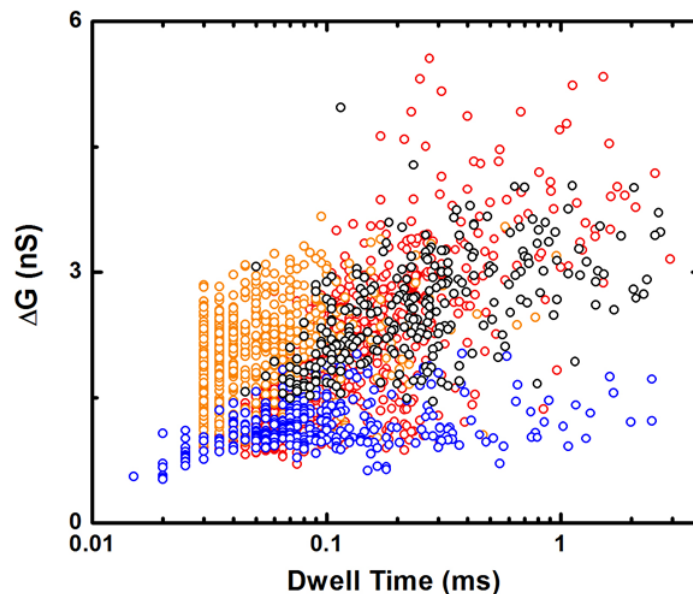


**Figure 5.2. Event duration versus mean conductance blockade.** Using a 12 nm pore and a 400 mV applied voltage, the following translocations were measured: 61 bp DNA (79.2 ng/ $\mu$ l, red circles), 61 b DNA (39.6 ng/ $\mu$ l, blue circles), SSB (44.7 ng/ $\mu$ l, black circles), 61 b DNA (39.6 ng/ $\mu$ l) incubated with SSB (112 ng/ $\mu$ l) (orange circles). Each population represents more than 200 individual events.

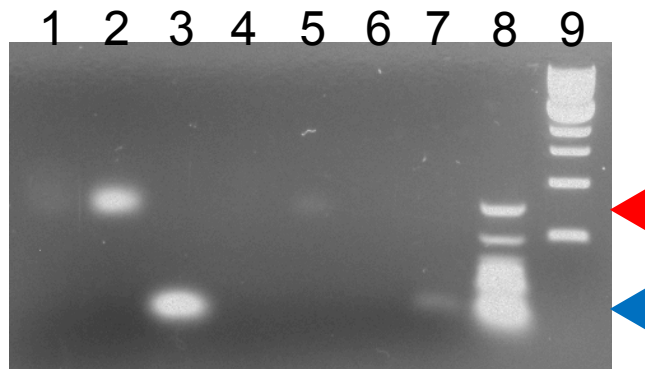


**Figure 5.3. Gel analysis of 61-mer ssDNA mixed with SSB.** Gel electrophoresis results after incubating SSB (559 ng/ $\mu$ l) with either 61 b heteropolymeric DNA (ssDNA) or T-homopolymeric DNA (TssDNA). Lane 1: SSB+ssDNA (99 ng/ $\mu$ l); lane 2: SSB+ssDNA (198 ng/ $\mu$ l); lane 3: ssDNA (297 ng/ $\mu$ l); lane 4: SSB+TssDNA (99 ng/ $\mu$ l); lane 5: SSB+TssDNA (198 ng/ $\mu$ l); lane 6: TssDNA (297 ng/ $\mu$ l); lane 7: 61 bp dsDNA (297 ng/ $\mu$ l); lanes 8 & 9: molecular weight ladders. The red arrow indicates the position of 766 bp DNA; the blue arrow indicates the position of 61 bp DNA.

To further investigate the structure of the DNA-SSB complex, a titration experiment was performed in which the amount of SSB was increased from 0 ng to ~ 2240 ng while the amount of ssM13 was held constant at 25 ng throughout. As shown in Figure 5.2a, additional amounts of SSB produced increasingly larger mean  $\Delta G$  values. This trend follows from the fact that a larger number of SSBs present in the reaction mixture results in a larger number of proteins bound to each ssDNA until the SSB concentration reaches saturation. The presence of a single population in each result, except the final ssDNA:SSB molar ratio, indicates a uniform reaction mixture in which the SSB concentration is the limiting component. As the SSB concentration increases across this reaction series, a larger range of DNA-SSB structures is made possible, as shown by the width of

the population. When the amount of SSB reaches a threshold level, which occurs somewhere between 224 ng and 2240 ng (bottom panel), a second population becomes evident, presumably due to the presence of excess SSB.

In previous work, enzyme digestion and electron microscopy analyses showed support for a repeating “SSB nucleosome” structure (81). SSB octamers, made up of two tetramers that occlude 145-170 DNA bases and flanked by ~ 30 unbound bases, are believed to be part of the core structural unit. SSB tetramers occur in alternation with these octamers in an equilibrium state. Using this model, ~ 80 SSBs might be expected to bind to a single ssM13 molecule. In Figure 5.2, the most shifted single population (second to last panel) represents ~ 284 SSBs/ssDNA, more than 3.5 times the amount that should be necessary under ideal reaction conditions for full DNA saturation. This difference may reflect a combination of factors, including the presence of inactive SSB, aggregation of SSB due to high salt conditions, and DNA secondary structures that limit SSB access.

The same titration series was prepared for bulk analysis using a gel electrophoretic shift assay. Visual inspection of the gel image (Fig. 5.2b inset) shows a similar trend in which a larger amount of SSB in the mixture results in a larger band shift. Bands also appear to be more “smeared” with increasing SSB concentration because the range of possible DNA-SSB structures increases, causing the DNA to be distributed over a larger migration distance. This effect corresponds to the wider populations observed in single molecule measurements

above. To quantify this shift, band intensity profiles were measured as a function of band migration distance; smaller brightness peaks appear at higher SSB concentrations since less DNA is available for dye intercalation as it becomes more occluded by bound SSB. When mean  $\Delta G$  values from our nanopore measurements are compared directly with band positions in the gel, the data follow almost identical distributions that resemble sigmoidal profiles. Many other natural processes demonstrate similar kinetic properties, including many classes of enzymes (82).

The interaction between SSB and ssDNA has been described using two types of nearest-neighbor cooperative binding models: an “unlimited” cooperativity process and a “limited” cooperativity process (77). “Unlimited” cooperativity is typical of the  $(SSB)_{35}$  mode, which is characterized by continuous clusters of tetramers that can saturate the ssDNA because nearest-neighbor interactions can occur on both sides of bound tetramers. In contrast, the high-salt binding kinetics of the  $(SSB)_{65}$  mode results in limited cooperativity (83). Since all four subunits are involved, protein clustering is limited to the formation of non-contiguous octamers from dimers of tetramers, resulting in discontinuous protein clusters that do not saturate the DNA (Fig. 5.4) (77). Since SSB binding is nonspecific in either case, low protein concentrations have little effect on the overall ssDNA topology. Thus, binding does occur in the SSB-limited regime (> 1:114 ratio), but the resulting structural changes do not significantly alter electrokinetic translocation through either the SS-nanopore or the gel. Above this

threshold value, SSB facilitates substantial nucleoprotein formation along the ssDNA until the reaction plateaus as the number of bound proteins reaches the maximum permitted under  $(SSB)_{65}$  mode limited cooperativity conditions.

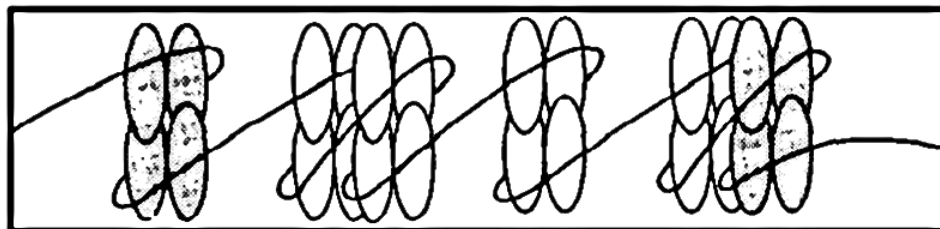


**Figure 5.4. Diagram of the  $(SSB)_{65}$  binding mode (77).** In this model of limited cooperativity, all four subunits of the SSB tetramer interact with ssDNA to form a nucleoprotein complex that can dimerize with one of its nearest neighbors into higher order octamers, resulting in a discontinuous chain of protein clusters.

Additional experiments using dsM13, equal in length to ssM13, emphasize the degree to which SSB can mediate differences between ds- and ssDNA and also serve as a control to assess the specificity of the ssDNA-SSB binding reaction. A separate analysis of dsDNA translocation measurements provides a mean  $\Delta G$  of  $1.8 \pm 0.3$  nS (Fig. 5.3a), very close to the 2.1 nS value obtained for ssDNA in our experimental conditions. Combining SSB with ssDNA, however, generates a complex that effectively shifts the mean  $\Delta G$  to  $12.7 \pm 4.4$  nS, making differences between ds- and ssDNA much more obvious. When dsDNA, ssDNA and SSB are mixed together in a single reaction (Fig. 5.3b), two populations emerge with mean  $\Delta G$  values corresponding to dsDNA and the ssDNA-SSB complex, as in (a). In addition, only enough SSB was used in both cases to fully

react with the ssDNA and effect a full shift, so the low population is not attributable to excess SSB.

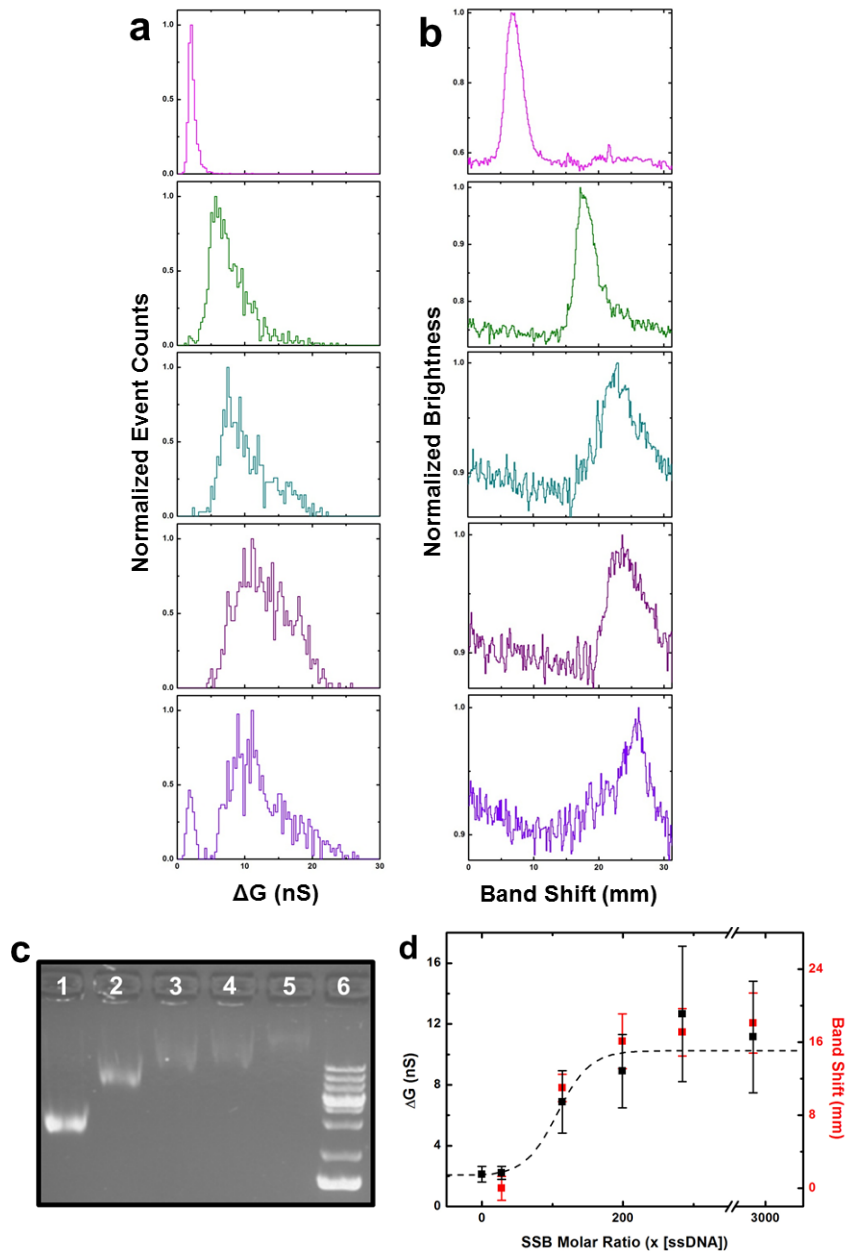


**Figure 5.5. Titration series mixtures of ssDNA and SSB.** (a) Event conductance blockade histograms of ssDNA incubated with SSB at different relative concentrations. From top to bottom, ssDNA (2.5 ng/ $\mu$ l) plus SSB as follows: 2.2 ng/ $\mu$ l ( $n = 989$ ), 8.9 ng/ $\mu$ l ( $n = 1048$ ), 15.6 ng/ $\mu$ l ( $n = 682$ ), 22.4 ng/ $\mu$ l ( $n = 824$ ), 224 ng/ $\mu$ l ( $n = 961$ ). (b) Brightness analysis plots of gel band versus migration distance corresponding to lanes 1 - 5 of gel image in (c). (d) Co-plot of mean  $\Delta G$  and relative band location.

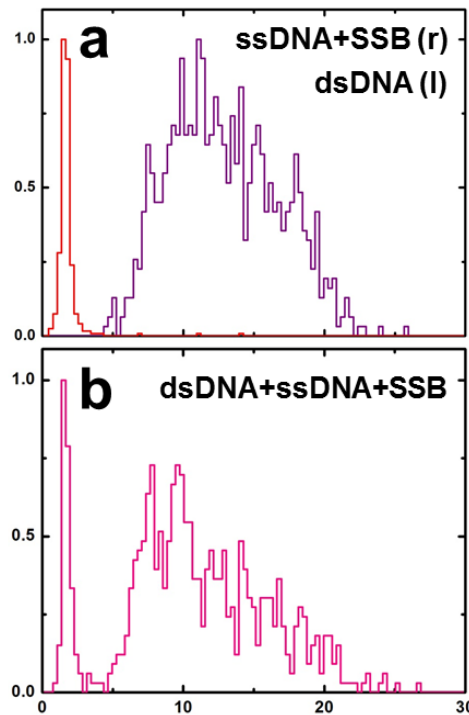


**Figure 5.6. Comparison of dsDNA and ssDNA+SSB.** (a) Overlaid event conductance blockade histograms of dsDNA (2.5 ng/ $\mu$ l,  $n = 333$ ) and ssDNA (2.5 ng/ $\mu$ l) incubated with SSB (22.4 ng/ $\mu$ l) at a molar ratio (ssDNA:SSB) of 1:284 ( $n = 824$ ), each measured separately. (b) Event conductance blockade histogram of dsDNA (2.5 ng/ $\mu$ l), ssDNA (2.5 ng/ $\mu$ l) and SSB (22.4 ng/ $\mu$ l) incubated together in a single-pot reaction at a molar ratio (dsDNA:ssDNA:SSB) of 1:1:284 ( $n = 675$ ) showing two discrete populations as in (a).

As discussed above, the most probable binding mode is  $(SSB)_{65}$ , given the high salt conditions of the measurement electrolyte. In this mode, the SSB tetramer occludes 65 nucleotides that wrap around the outside of the protein to form a complex that exhibits a limited nearest-neighbor cooperativity (84). In this interaction, continuous protein clusters are absent; instead, an equilibrium state exists between bound tetramers and higher-order octameric structures that are

formed when adjacent tetramers join together. An important consequence of this type of interaction is the presence of larger local structures along the ssDNA polynucleotide, causing much deeper conductance blockades than bound tetramers would individually. A second important consequence is that higher order substructures further hinder the formation of large entropic coils since open ssDNA regions are removed and secondary structures typical of large ssDNA, which can be extensive, are minimized.

All measurements thus far have been performed on circular DNA, which is intrinsically limited in folding conformation due to its continuous nature. As a result, even when fully saturated with SSB, these molecules should be incapable of translocating through a SS-nanopore with fewer than two strands simultaneously. We therefore expect that a linearized ssDNA molecule, especially its SSB-saturated form, should yield a wider range of accessible event depths. For example, a single nucleoprotein filament would be able to translocate through the pore instead of two parallel filaments.

To test this hypothesis, we performed translocations using a mixture containing linearized ssM13 and SSB. These results, summarized in Figure 5.4b, show a high degree of similarity to circular ssM13 coated with SSB (Fig. 5.4a). The most notable difference is the presence of a second population, which is believed to represent excess SSB since the available concentration of linear ssDNA was much lower after enzymatic processing and purification losses. A gel analysis (Fig. 5.4) confirms that bare DNA migrates very differently, depending

on whether it is circular ssDNA (lane 2), linearized ssDNA (lane 3), or dsDNA (lane 4). Despite their apparent differences, the introduction of SSB drives an “organizing” process in which complex formation forces an unfolded DNA topology of bound tetramers and octamers separated by short DNA linkers, attenuating structural differences between circular and linearized ssM13.

Given the diameter of our nanopores ( $\sim 12$  nm) and the size of the DNA-SSB complex ( $> 8$  nm), it seems likely that these measurements reflect the passage of bound SSB tetramers or octamers in single file fashion, regardless of whether or not the ssDNA is circular or linear. This also explains the high level of similarity between the two. For circular ssM13-SSB measurements, this would mean the simultaneous translocation of two strands, with SSB coupled to one or the other. With linearized ssM13-SSB, however, translocations of single strands complexed with SSB can occur, resulting in slightly smaller conductance changes and longer translocation durations. These differences represent the volume excluded by a single DNA strand and roughly twice the length of circular ssM13. In fact, event duration histograms are quite different, showing a mean  $\Delta t$  of  $\sim 78 \pm 20 \mu\text{s}$  for circular ssM13-SSB and  $\sim 117 \pm 27 \mu\text{s}$  for linearized ssM13-SSB, although mean conductance blockades differ by only 1 nS.

Their relative electrokinetic properties may also be influenced by the density and mobility of bound proteins. In a single molecule fluorescence resonance energy transfer (smFRET) study, the ssDNA-SSB complex was discovered to be highly dynamic, capable of repositioning itself in a random walk

along the DNA (85). Since SSB migration is a rapid, spontaneous process, this may provide a mechanism that facilitates their translocation by preventing bound tetramers from stacking up against each other at the pore entrance.

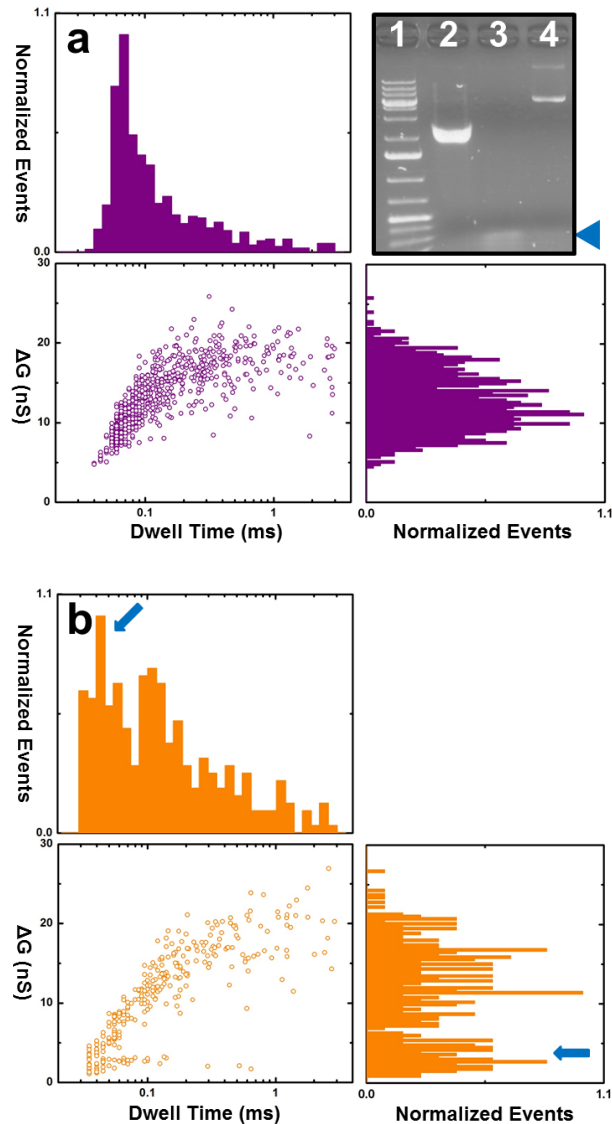


**Figure 5.7. Circular ssDNA+SSB and linearized ssDNA+SSB.** (a) Scatter plot of event duration versus conductance blockade for circular ssDNA (2.5 ng/ $\mu$ l) incubated with SSB (22.4 ng/ $\mu$ l) with event  $\Delta G$  and  $\Delta t$  histograms (n = 824). Gel image showing relative migration of circular ssDNA (lane 2), linear ssDNA (lane 3) and dsDNA (lane 4). The red arrow indicates the position of 7.2 kb linear ssDNA. (b) Scatter plot of event duration versus conductance blockade for linearized ssDNA (0.4 ng/ $\mu$ l) incubated with SSB (22.4 ng/ $\mu$ l) with event  $\Delta G$  and  $\Delta t$  histograms (n = 306). The blue arrows indicate a second population of events characterized by smaller conductance blockades and shorter event durations.

## CHAPTER VI

### CONCLUSIONS

SS-nanopores offer many desirable features as highly sensitive measurement systems. Pore dimensions can be precisely controlled to fit the application; they are very robust and tolerate repeated testing, permitting long-term use; their stability is very high across a wide range of experimental conditions; and they require minimal storage costs (25). Parallel fabrication strategies are also becoming practical using advanced systems, such as the HIM, which performs with high precision, thus ensuring high quality control of SS-nanopores. Although equipment needs are minor and samples require little preparation, SS-nanopores are showing great potential across fields, such as genotyping or biomarker discovery, due to their major advantage as single molecule detection platforms.

#### Membrane Thinning Techniques for Nanopore Fabrication

We have demonstrated that the beam of a HIM can be used to control the thickness of a free-standing silicon nitride membrane. From topographical data obtained with AFM on both the side of ion beam incidence (direct-milling) and the opposite side (transmission-milling), we were able to reconstruct the complete profiles of milled membranes. We found that the surface surrounding the milling pattern was depressed on the direct side and enhanced on the transmission side,

leading us to speculate that fluidization and ion pressure affect the surface immediately adjacent to the patterned areas. By measuring milled depth relative to the unmodified membrane, we were able to quantify the material removal rate on both sides of the membrane during ion beam exposure, finding a linear relationship with dose in direct-milling and a dependence on the square of the dose in transmission-milling. This resulted in an extrapolated relationship between the total ion dose and the remaining membrane thickness. This finding can be used to predict the remaining thickness of a membrane for a given dose of incident ions. We expect this technique will be useful in various applications, such as plasmonic devices (40,86), graphene patterning (41,42), and one-step fabrication of solid-state nanopores (5) in ultrathin membranes.

#### Detecting DNA Depurination

We have demonstrated that SS-nanopores can be used to characterize depurination in short duplex DNA molecules. We used low pH conditions to hydrolyze glycosidic bonds in 61 bp DNA, releasing purine nucleotides in the process. We found that this degradation produced significant increases in the duration of conductance blockades, showing that depurinated DNA translocates up to an order of magnitude more slowly than undamaged molecules, on average. This observation was attributed to a progressive loss of the double-stranded helix, which intensifies confinement effects due to open regions of single-stranded structure where unpaired nucleotides can come into direct

contact with the SS-nanopore. This facilitates stronger interactions between threading molecules and the pore, inhibiting translocation speeds.

Our approach is fast, label-free, and can be used for a coarse determination of either the overall level of depurination within a collection of dsDNA or the degradation of individual translocating molecules. While assumptions are currently required for this type of characterization, further study of the system will enable direct quantification of abasic sites. Given that depurination is a continual process, this detection technique could have useful applications in a wide variety of fields that rely on DNA analyses, including forensics. Finally, since AP sites can lead to the initiation of diseases, such as cancer, SS-nanopore detection of depurination may have future clinical relevance as a diagnostic tool.

#### Using Single-Stranded DNA Binding Proteins to Differentiate Double- and Single-Stranded DNA

During the last few years, many worthwhile SS-nanopore applications have been explored. One potentially important direction that is beginning to receive attention is early-stage medical diagnosis, such as single molecule detection of HIV-1 protein biomarkers (87). As these and other new approaches are refined to meet high sensitivity, specificity and throughput requirements, SS-nanopores may also be developed as a DNA biomarker discovery platform. The work presented here may represent an important step because it demonstrates

that a protein-binding assay with high specificity and affinity for ssDNA can be used as an effective screening tool to analyze heterogeneous DNA samples.

Binding of SSB protects and stabilizes ssDNA and the (SSB)<sub>65</sub> binding mode, in particular, generates a periodic nucleoprotein structure throughout the DNA polynucleotide. The resulting equilibrium structure is both shorter and bulkier than naked ssDNA, comprising a chain of bound SSB tetramers and octamers separated by short DNA linkers ~ 30 bases long (81). Translocations of this complex produce characteristic conductance blockades that are much deeper and event durations that are much longer than unbound ssDNA, SSB or dsDNA equal in length.

In a newly released report, DNA-SSB complexes were probed using much larger SS-nanopores (20-50 nm) under similar experimental conditions (88). Their experimental results indicate a much lower binding density of SSB along the ssDNA and only minor deviations from unbound DNA measurements. In contrast, our much smaller pores were able to register very large shifts in the electrical characteristics of these nucleoproteins, emphasizing the importance of tuning the nanopore size in order to maximize sensitivity.

Such large shifts in electrokinetic behavior associated with DNA-SSB interactions make it possible to easily identify the presence of ssDNA targets, without the need for binding in a sequence-dependent manner. Preliminary processing of a DNA sample could include fragmentation and denaturation steps and subsequently passing the sample over a column containing a

complementary sequence of the biomarker. This serves as a filtration step to remove one of the biomarker strands from the flow-through sample, resulting in a mixed sample of ds- and biomarker ssDNA. Addition of SSB in a final preparatory step would then yield a sample that is ready to be probed using SS-nanopores. As demonstrated by the results discussed above, the resulting translocation data can be analyzed for characteristic electronic signatures that clearly differentiate SSB-bound DNA biomarkers from a background mixture of unbound protein and dsDNA.

## Bibliography

1. Wanunu, M. (2012) Nanopores: A journey towards DNA sequencing. *Physics of Life Reviews*, **9**, 125-158.
2. Kasianowicz, J.J., Brandin, E., Branton, D. and Deamer, D.W. (1996) Characterization of individual polynucleotide molecules using a membrane channel. *Proceedings of the National Academy of Sciences of the United States of America*, **93**, 13770-13773.
3. Li, J., Stein, D., McMullan, C., Branton, D., Aziz, M.J. and Golovchenko, J.A. (2001) Ion-beam sculpting at nanometre length scales. *Nature*, **412**, 166-169.
4. Storm, A.J., Chen, J.H., Zandbergen, H.W. and Dekker, C. (2005) Translocation of double-strand DNA through a silicon oxide nanopore. *Physical Review E*, **71**, 10.
5. Yang, J.J., Ferranti, D.C., Stern, L.A., Sanford, C.A., Huang, J., Ren, Z., Qin, L.C. and Hall, A.R. (2011) Rapid and precise scanning helium ion microscope milling of solid-state nanopores for biomolecule detection. *Nanotechnology*, **22**.
6. Li, J.L., Gershow, M., Stein, D., Brandin, E. and Golovchenko, J.A. (2003) DNA molecules and configurations in a solid-state nanopore microscope. *Nature Materials*, **2**, 611-615.
7. Plesa, C., Kowalczyk, S.W., Zinsmeister, R., Grosberg, A.Y., Rabin, Y. and Dekker, C. (2013) Fast Translocation of Proteins through Solid State Nanopores. *Nano Letters*, **13**, 658-663.
8. Skinner, G.M., van den Hout, M., Broekmans, O., Dekker, C. and Dekker, N.H. (2009) Distinguishing Single- and Double-Stranded Nucleic Acid Molecules Using Solid-State Nanopores. *Nano Letters*, **9**, 2953-2960.
9. Kowalczyk, S.W., Hall, A.R. and Dekker, C. (2010) Detection of Local Protein Structures along DNA Using Solid-State Nanopores. *Nano Letters*, **10**, 324-328.

10. Smeets, R.M.M., Kowalczyk, S.W., Hall, A.R., Dekker, N.H. and Dekker, C. (2009) Translocation of RecA-Coated Double-Stranded DNA through Solid-State Nanopores. *Nano Letters*, **9**, 3089-3095.
11. Singer, A., Rapireddy, S., Ly, D.H. and Meller, A. (2012) Electronic barcoding of a viral gene at the single-molecule level. *Nano Letters*, **12**, 1722-1728.
12. Wanunu, M., Sutin, J. and Meller, A. (2009) DNA Profiling Using Solid-State Nanopores: Detection of DNA-Binding Molecules. *Nano Letters*, **9**, 3498-3502.
13. Wanunu, M., Cohen-Karni, D., Johnson, R.R., Fields, L., Benner, J., Peterman, N., Zheng, Y., Klein, M.L. and Drndic, M. (2011) Discrimination of Methylcytosine from Hydroxymethylcytosine in DNA Molecules. *Journal of the American Chemical Society*, **133**, 486-492.
14. Shim, J., Humphreys, G.I., Venkatesan, B.M., Munz, J.M., Zou, X.Q., Sathe, C., Schulten, K., Kosari, F., Nardulli, A.M., Vasmatzis, G. *et al.* (2013) Detection and Quantification of Methylation in DNA using Solid-State Nanopores. *Scientific Reports*, **3**.
15. Carlsen, A.T., Zahid, O.K., Ruzicka, J.A., Taylor, E.W. and Hall, A.R. (2014) Selective Detection and Quantification of Modified DNA with Solid-State Nanopores. *Nano Lett.*
16. Jacinto, F.V., Ballestar, E. and Esteller, M. (2008) Methyl-DNA immunoprecipitation (MeDIP): hunting down the DNA methylome. *Biotechniques*, **44**, 35, 37, 39 passim.
17. Laird, P.W. (2010) Principles and challenges of genomewide DNA methylation analysis. *Nat Rev Genet*, **11**, 191-203.
18. Williams, K., Christensen, J., Pedersen, M.T., Johansen, J.V., Cloos, P.A., Rappsilber, J. and Helin, K. (2011) TET1 and hydroxymethylcytosine in transcription and DNA methylation fidelity. *Nature*, **473**, 343-348.
19. Song, C.X., Yi, C. and He, C. (2012) Mapping recently identified nucleotide variants in the genome and transcriptome. *Nat Biotechnol*, **30**, 1107-1116.
20. Hirai, M.Y., Klein, M., Fujikawa, Y., Yano, M., Goodenowe, D.B., Yamazaki, Y., Kanaya, S., Nakamura, Y., Kitayama, M., Suzuki, H. *et al.*

- (2005) Elucidation of gene-to-gene and metabolite-to-gene networks in arabidopsis by integration of metabolomics and transcriptomics. *J Biol Chem*, **280**, 25590-25595.
21. Zhao, J., Ohsumi, T.K., Kung, J.T., Ogawa, Y., Grau, D.J., Sarma, K., Song, J.J., Kingston, R.E., Borowsky, M. and Lee, J.T. (2010) Genome-wide identification of polycomb-associated RNAs by RIP-seq. *Mol Cell*, **40**, 939-953.
  22. Peng, J., Schwartz, D., Elias, J.E., Thoreen, C.C., Cheng, D., Marsischky, G., Roelofs, J., Finley, D. and Gygi, S.P. (2003) A proteomics approach to understanding protein ubiquitination. *Nat Biotechnol*, **21**, 921-926.
  23. Rual, J.F., Venkatesan, K., Hao, T., Hirozane-Kishikawa, T., Dricot, A., Li, N., Berriz, G.F., Gibbons, F.D., Dreze, M., Ayivi-Guedehoussou, N. *et al.* (2005) Towards a proteome-scale map of the human protein-protein interaction network. *Nature*, **437**, 1173-1178.
  24. Zhang, B., Park, B.H., Karpinets, T. and Samatova, N.F. (2008) From pull-down data to protein interaction networks and complexes with biological relevance. *Bioinformatics*, **24**, 979-986.
  25. Storm, A.J., Storm, C., Chen, J.H., Zandbergen, H., Joanny, J.F. and Dekker, C. (2005) Fast DNA translocation through a solid-state nanopore. *Nano Letters*, **5**, 1193-1197.
  26. Smeets, R.M.M., Keyser, U.F., Krapf, D., Wu, M.Y., Dekker, N.H. and Dekker, C. (2006) Salt dependence of ion transport and DNA translocation through solid-state nanopores. *Nano Letters*, **6**, 89-95.
  27. Kowalczyk, S.W., Wells, D.B., Aksimentiev, A. and Dekker, C. (2012) Slowing down DNA Translocation through a Nanopore in Lithium Chloride. *Nano Letters*, **12**, 1038-1044.
  28. Wanunu, M., Morrison, W., Rabin, Y., Grosberg, A.Y. and Meller, A. (2010) Electrostatic focusing of unlabelled DNA into nanoscale pores using a salt gradient. *Nature Nanotechnology*, **5**, 160-165.
  29. Fologea, D., Uplinger, J., Thomas, B., McNabb, D.S. and Li, J.L. (2005) Slowing DNA translocation in a solid-state nanopore. *Nano Letters*, **5**, 1734-1737.

30. Fologea, D., Gershow, M., Ledden, B., McNabb, D.S., Golovchenko, J.A. and Li, J.L. (2005) Detecting single stranded DNA with a solid state nanopore. *Nano Letters*, **5**, 1905-1909.
31. Marshall, M.M., Ruzicka, J.A., Taylor, E.W. and Hall, A.R. (2014) Detecting DNA depurination with solid-state nanopores. *PLoS One*, **9**, e101632.
32. Wanunu, M., Sutin, J., McNally, B., Chow, A. and Meller, A. (2008) DNA Translocation Governed by Interactions with Solid-State Nanopores. *Biophysical Journal*, **95**, 4716-4725.
33. Marshall, M.M., Yang, J. and Hall, A.R. (2012) Direct and transmission milling of suspended silicon nitride membranes with a focused helium ion beam. *Scanning*, **34**, 101-106.
34. Wanunu, M., Dadosh, T., Ray, V., Jin, J.M., McReynolds, L. and Drndic, M. (2010) Rapid electronic detection of probe-specific microRNAs using thin nanopore sensors. *Nature Nanotechnology*, **5**, 807-814.
35. Morgan J., N.J., Hill R., Ward B. . (2006) An introduction to the helium ion microscope. *Microscopy Today*, **14**, 24-31.
36. Scipioni L., S.L.A., Notte J., Sijbrandij S., Griffin B. (2008) Helium ion microscope. *Advanced Materials and Processes*, **166**, 27-30.
37. Ramachandra, R., Griffin, B. and Joy, D. (2009) A model of secondary electron imaging in the helium ion scanning microscope. *Ultramicroscopy*, **109**, 748-757.
38. Scipioni L., A.P., Sidorkin V., Chen P., Maas D., et al. (2009) The helium ion microscope: Advances in technology and applications. *American Laboratory*, **41**, 26-28.
39. Bazou, D., Behan, G., Reid, C., Boland, J.J. and Zhang, H.Z. (2011) Imaging of human colon cancer cells using He-Ion scanning microscopy. *J Microsc*, **242**, 290-294.
40. Scipioni L., F.D.C., Smentkowski V. S., Potyrailo R. A. (2010) Fabrication and initial characterization of ultrahigh aspect ratio vias in gold using the helium ion microscope. *Journal of Vacuum Science & Technology B*, **28**, C6P18-C16P23.

41. Bell, D.C., Lemme, M.C., Stern, L.A., Williams, J.R. and Marcus, C.M. (2009) Precision cutting and patterning of graphene with helium ions. *Nanotechnology*, **20**, 455301.
42. Lemme, M.C., Bell, D.C., Williams, J.R., Stern, L.A., Baugher, B.W.H., Jarillo-Herrero, P. and Marcus, C.M. (2009) Etching of Graphene Devices with a Helium Ion Beam. *Acs Nano*, **3**, 2674-2676.
43. Ishitani T., T.H., Yaguchi T., Koike H. (1994) Transmission electron-microscope sample preparation using a focused ion-beam. *Journal of Electron Microscopy*, **43**, 322-326.
44. Mitsui, T., Stein, D., Kim, Y.R., Hoogerheide, D. and Golovchenko, J.A. (2006) Nanoscale volcanoes: accretion of matter at ion-sculpted nanopores. *Phys Rev Lett*, **96**, 036102.
45. Storm, A.J., Chen, J.H., Ling, X.S., Zandbergen, H.W. and Dekker, C. (2003) Fabrication of solid-state nanopores with single-nanometre precision. *Nat Mater*, **2**, 537-540.
46. Tseng, A.A. (2005) Recent developments in nanofabrication using focused ion beams. *Small*, **1**, 924-939.
47. Dai T., K.X., Zhang B., Xu J., Bao K., et al. (2008) Study and formation of 2D microstructures of sapphire by focused ion beam milling. *Microelectronic Engineering*, **85**, 640-645.
48. R., B. (1981) *Sputtering by Particle Bombardment I: Physical Sputtering of Single-Element Solids*. Springer-Verlag, Berlin.
49. Tseng, A.A. (2004) Recent developments in micromilling using focused ion beam technology. *Journal of Micromechanics and Microengineering*, **14**, R15-R34.
50. Bay H. L., A.H.H., Hofer W. O. (1976a) Transmission sputtering as a technique for measuring distribution of energy deposited in solids by ion-bombardment. *Radiation Effects and Defects in Solids*, **S 28**, 87-95.
51. Bay H. L., A.H.H., Hofer W. O., Nielsen O. (1976b) Transmission sputtering yields of gold at 6.8 MeV. *Journal of Applied Physics*, **11**, 289-293.

52. Lindahl, T. (1993) Instability and Decay of the Primary Structure of DNA. *Nature*, **362**, 709-715.
53. Lindahl, T. and Nyberg, B. (1972) Rate of Depurination of Native Deoxyribonucleic Acid. *Biochemistry*, **11**, 3610-&.
54. Amosova, O., Coulter, R. and Fresco, J.R. (2006) Self-catalyzed site-specific depurination of guanine residues within gene sequences. *Proceedings of the National Academy of Sciences of the United States of America*, **103**, 4392-4397.
55. Cavaliere, E., Saeed, M., Zahid, M., Cassada, D., Snow, D., Miljkovic, M. and Rogan, E. (2012) Mechanism of DNA depurination by carcinogens in relation to cancer initiation. *lubmb Life*, **64**, 169-179.
56. Boiteux, S. and Guillet, M. (2004) Abasic sites in DNA: repair and biological consequences in *Saccharomyces cerevisiae*. *DNA Repair*, **3**, 1-12.
57. Alvarez-Dominguez, J.R., Amosova, O. and Fresco, J.R. (2013) Self-catalytic DNA Depurination Underlies Human beta-Globin Gene Mutations at Codon 6 That Cause Anemias and Thalassemias. *Journal of Biological Chemistry*, **288**, 11581-11589.
58. Freese, E.B. (1961) Transitions and Transversions Induced by Depurinating Agents. *Proceedings of the National Academy of Sciences of the United States of America*, **47**, 540-&.
59. Yakes, F.M. and VanHouten, B. (1997) Mitochondrial DNA damage is more extensive and persists longer than nuclear DNA damage in human cells following oxidative stress. *Proceedings of the National Academy of Sciences of the United States of America*, **94**, 514-519.
60. Abdullin, T.I., Nikitina, I. and Bondar, O.V. (2008) Detection of DNA depurination with the use of an electrode modified with carbon nanotubes. *Journal of Analytical Chemistry*, **63**, 690-692.
61. Evers, D.L., Fowler, C.B., Cunningham, R.E., Mason, J.T. and O'Leary, T.J. (2007) A novel HPLC method reveals that precipitation of 2'-deoxyadenosine 5'-monophosphate with lithium perchlorate/acetone leads to base depurination. *Analytical Biochemistry*, **370**, 255-257.

62. Iacono, J.A., Gildea, B. and McLaughlin, L.W. (1990) Mild Acid-Hydrolysis of 2-Pyrimidinone-Containing DNA Fragments Generates Apurinic Apyrimidinic Sites. *Tetrahedron Letters*, **31**, 175-178.
63. Nakamura, J., Walker, V.E., Upton, P.B., Chiang, S.Y., Kow, Y.W. and Swenberg, J.A. (1998) Highly sensitive apurinic/apyrimidinic site assay can detect spontaneous and chemically induced depurination under physiological conditions. *Cancer Research*, **58**, 222-225.
64. An, N., Fleming, A.M., White, H.S. and Burrows, C.J. (2012) Crown ether-electrolyte interactions permit nanopore detection of individual DNA abasic sites in single molecules. *Proceedings of the National Academy of Sciences of the United States of America*, **109**, 11504-11509.
65. Dekker, C. (2007) Solid-state nanopores. *Nature Nanotechnology*, **2**, 209-215.
66. Healy, K. (2007) Nanopore-based single-molecule DNA analysis. *Nanomedicine*, **2**, 459-481.
67. Tamm, C., Hodes, M.E. and Chargaff, E. (1952) The Formation of Apurinic Acid from the Desoxyribonucleic Acid of Calf Thymus *The Journal of Biological Chemistry*, **195**, 15.
68. Southern, E.M. (1975) Detection of Specific Sequences among DNA Fragments Separated by Gel-Electrophoresis. *Journal of Molecular Biology*, **98**, 503-&.
69. Lindahl, T. and Andersso.A. (1972) Rate of Chain Breakage at Apurinic Sites in Double-Stranded Deoxyribonucleic Acid. *Biochemistry*, **11**, 3618-&.
70. Firnkens, M., Pedone, D., Knezevic, J., Doeblinger, M. and Rant, U. (2010) Electrically Facilitated Translocations of Proteins through Silicon Nitride Nanopores: Conjoint and Competitive Action of Diffusion, Electrophoresis, and Electroosmosis. *Nano Letters*, **10**, 2162-2167.
71. Manning, G.S. (1978) The molecular theory of polyelectrolyte solutions with applications to the electrostatic properties of polynucleotides. *Quarterly Reviews of Biophysics*, **11**, 68.
72. Anderson, B.N., Muthukumar, M. and Meller, A. (2013) pH Tuning of DNA Translocation Time through Organically Functionalized Nanopores. *Acs Nano*, **7**, 1408-1414.

73. Kowalczyk, S.W., Tuijtel, M.W., Donkers, S.P. and Dekker, C. (2010) Unraveling Single-Stranded DNA in a Solid-State Nanopore. *Nano Letters*, **10**, 1414-1420.
74. Akahori, R., Haga, T., Hatano, T., Yanagi, I., Ohura, T., Hamamura, H., Iwasaki, T., Yokoi, T. and Anazawa, T. (2014) Slowing single-stranded DNA translocation through a solid-state nanopore by decreasing the nanopore diameter. *Nanotechnology*, **25**, 275501.
75. Soni, G.V. and Dekker, C. (2012) Detection of Nucleosomal Substructures using Solid-State Nanopores. *Nano Letters*, **12**, 3180-3186.
76. Meyer, R.R. and Laine, P.S. (1990) The single-stranded DNA-binding protein of Escherichia coli. *Microbiol Rev*, **54**, 342-380.
77. Lohman, T.M. and Ferrari, M.E. (1994) Escherichia coli single-stranded DNA-binding protein: multiple DNA-binding modes and cooperativities. *Annu Rev Biochem*, **63**, 527-570.
78. Molineux, I.J. and Gefter, M.L. (1974) Properties of the Escherichia coli in DNA binding (unwinding) protein: interaction with DNA polymerase and DNA. *Proc Natl Acad Sci U S A*, **71**, 3858-3862.
79. Weiner, J.H., Bertsch, L.L. and Kornberg, A. (1975) The deoxyribonucleic acid unwinding protein of Escherichia coli. Properties and functions in replication. *J Biol Chem*, **250**, 1972-1980.
80. Fologea, D., Ledden, B., McNabb, D.S. and Li, J.L. (2007) Electrical characterization of protein molecules by a solid-state nanopore. *Applied Physics Letters*, **91**.
81. Chrysogelos, S. and Griffith, J. (1982) Escherichia coli single-strand binding protein organizes single-stranded DNA in nucleosome-like units. *Proc Natl Acad Sci U S A*, **79**, 5803-5807.
82. R., C. (2005) *Physical Chemistry for the Biosciences*. University Science Books, California, USA.
83. Overman, L.B. and Lohman, T.M. (1994) Linkage of pH, anion and cation effects in protein-nucleic acid equilibria. Escherichia coli SSB protein-single stranded nucleic acid interactions. *J Mol Biol*, **236**, 165-178.

84. Raghunathan, S., Kozlov, A.G., Lohman, T.M. and Waksman, G. (2000) Structure of the DNA binding domain of E. coli SSB bound to ssDNA. *Nat Struct Biol*, **7**, 648-652.
85. Roy, R., Kozlov, A.G., Lohman, T.M. and Ha, T. (2009) SSB protein diffusion on single-stranded DNA stimulates RecA filament formation. *Nature*, **461**, 1092-1097.
86. Genet, C. and Ebbesen, T.W. (2007) Light in tiny holes. *Nature*, **445**, 39-46.
87. Niedzwiecki, D.J., Iyer, R., Borer, P.N. and Movileanu, L. (2013) Sampling a Biomarker of the Human Immunodeficiency Virus across a Synthetic Nanopore. *Acs Nano*, **7**, 3341-3350.
88. Japrun, D., Bahrami, A., Nadzeyka, A., Peto, L., Bauerdick, S., Edel, J.B. and Albrecht, T. (2014) SSB Binding to Single-Stranded DNA Probed Using Solid-State Nanopore Sensors. *J Phys Chem B*.